8-7-2004

A Theoretical and Experimental Investigation of Power Transmission in a Large Diameter Optical Fiber

Frances D. Carter

A THEORETICAL AND EXPERIMENTAL INVESTIGATION OF POWER TRANSMISSION IN A LARGE DIAMETER OPTICAL FIBER

By

Frances D. Carter

A Thesis
Submitted to the Faculty of
Mississippi State University
in Partial Fulfillment of the Requirements
for the Degree of Master of Science
in Physics
in the Department of Physics and Astronomy

Mississippi State, Mississippi

August 2004

A THEORETICAL AND EXPERIMENTAL INVESTIGATION OF POWER TRANSMISSION IN A LARGE DIAMETER OPTICAL FIBER

By

Frances D. Carter

Approved:

John T. Foley Professor of Physics and Astronomy (Major Professor)	Jagdish P. Singh Research Professor, Diagnostic Instrumentation and Analysis Laboratory (Committee Member)
Taha Mzoughi Associate Professor of Physics and Astronomy (Committee Member)	David L. Monts Professor and Graduate Coordinator, Department of Physics and Astronomy

Phil Oldham
Dean of the College of Arts and Science

Name: Frances D. Carter

Date of Degree: August 7, 2004

Institution: Mississippi State University

Major Field: Physics

Major Professor: Dr. John T. Foley

Title of Study: A THEORETICAL AND EXPERIMENTAL INVESTIGATION OF POWER TRANSMISSION IN A LARGE DIAMETER OPTICAL FIBER

Pages in Study: 76

Candidate for Degree of Master of Science

The effect of varying the angle of incidence of a Gaussian beam from a He-Ne laser incident upon a large radius optical fiber is theoretically and experimentally investigated. The modes in a weakly-guiding, step index fiber were determined by using an analytical approximation technique to calculate the corresponding eigenvalues. An expression was developed for the fractional power per mode as a function of the angle of incidence for such a fiber. This expression was used to calculate the fractional power per mode for the lowest order 171 modes. This allowed the calculation of the fractional power per order and total power. By comparing these theoretical results to our experiment results, it is shown that the theoretical method is accurate at normal incidence and gives qualitative but not quantitative agreement at larger angles.

DEDICATION

To family and friends, both those who have been here since the beginning and those life has presented through blood, friendship and science.

ACKNOWLEDGMENTS

I would like to greatly thank DIAL for providing the financial support for this thesis. I would like to thank my advisors, Dr. John T. Foley and Dr. J.P. Singh for the support and learning they supplied that were necessary for me to complete this thesis. I would also like to thank Dr. Sunil Khijwania, Dr. Renat Letfullin and Tracy Miller for valuable help in the theoretical and experimental process. Also I thank Dr. David Monts and the Department of Physics and Astronomy at Mississippi State University for the opportunity.

TABLE OF CONTENTS

CHAPTER Page

LIST OF TABLES

LIST OF FIGURES

FIGURE Page

FIGURE Page

CHAPTER I

INTRODUCTION

Optical fibers are light transmitting devices, invented in the early 1970s, that have revolutionized the field of optics and allowed innovation in a range of fields, including but not limited to telecommunications and sensing. The ability of optical fibers to transmit low loss light signals over large distances is one of the most important aspects of the revolution. Although the applications of optical fibers are growing more complex, from the physicist's point of view the understanding of the fundamental physics is the key to developing new applications and advancing the technology. Therefore, in this thesis, we concentrate on understanding the fundamentals of varying launching conditions on power transmission in a weakly-guiding, step index fiber. Specifically, the effects of varying the angle of incidence on power transmission in a straight optical fiber with a 100μm core radius are investigated.

There are several conditions and assumptions in this thesis that will now be introduced. First, by "large radius" fiber, we mean fibers with a large normalized waveguide parameter, *V*. In practice, this means the fiber is highly multimode. Second, we will concentrate on the guided modes in the fiber, not the radiation modes. Third, the paraxial approximation is used throughout since we are only interested in small angles of

incidence. With the purpose and assumptions stated, the organization of this thesis is as follows:

In Chapter II, the basic concepts necessary to solve for the modes of optical fibers are introduced. The analytical approximation technique of Gloge [1] for the determination of the eigenvalues of weakly, guiding step index fibers is presented. Electric field and intensity distribution of the modes in an optical fiber are calculated and graphically illustrated.

In Chapter III, the effect of varying the angle of incidence on the power transmitted is investigated theoretically. A new expression for the power per mode as a function of the angle of incidence for optical fibers of large radius is derived. This result is used to calculate the fractional power per mode, power per order, and total power of the 100μm fiber used in the experiments discussed in Chapter IV. The theoretical results provide detailed information about the power distribution in the individual modes.

In Chapter IV we investigated experimentally the effect of varying the angle of incidence on the guided power in an optical fiber by describing the experiment and presenting its results. The experimental results agree qualitatively with the theoretical results for very small angles of incidence but not at larger angles. Possible reasons for this disagreement are discussed.

CHAPTER II

SOLUTIONS AND SIMULATIONS OF OPTICAL FIBER MODES

In this chapter the parameters of one type of fiber, the weakly-guiding step-index fiber, are introduced, and the techniques used to solve for the modes of such a fiber are presented. The modes of an optical fiber are solutions to Maxwell's equations that obey the appropriate boundary conditions. The modes are electric fields that maintain the same transverse distribution and polarization during propagation through the fiber. Understanding of the modes, which govern the light propagation in the fiber, is essential to the analysis of the fiber as well as the design of optical fiber systems. Ghatak [2] states that the calculation of the modal field distributions and the corresponding propagation constants are extremely important to the study of optical fibers. Specifically, knowledge of the modal field distribution is essential for the calculation of excitation efficiencies and splice losses at joints and the development of new fiber optic devices. In this thesis, modal analysis using an analytic approximation technique is investigated. The equations and relationships from the analytic approximation technique are used to solve for the specific eigenvalues of the modes. These eigenvalues are then input into modal equations to illustrate the optical fiber modes for given parameter sets.

2.1 Modal Analysis of an Optical Fiber

Consider a cylindrical dielectric waveguide defined by an inner material, the core with index of refraction n_1, surrounded by an outer material, the cladding of index of refraction n_2. The core radius, a, is illustrated in Fig. 2.1. The radius of the cladding is assumed to be large enough so that the effect of the air-cladding boundary on the light propagation in the fiber is negligible [3].

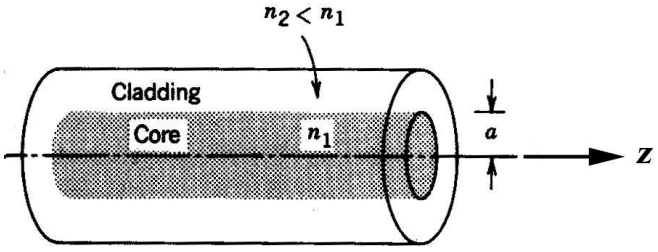

Figure 2.1 Cylindrical Dielectric Waveguide or Optical Fiber [from Ref. 3].

Step-index fibers, characterized by the following index of refraction profile [2],

$$n = \begin{cases} n_1, & 0 < r < a, \\ n_2, & r > a \end{cases} \tag{2.1}$$

are considered in this thesis. For most realistic fibers, the difference between the two indices of refraction is much smaller than the index of the core [1-4]. This relationship may be expressed as [3]

$$\Delta = \frac{n_1 - n_2}{n_1} << 1 \quad . \tag{2.2}$$

The maximum value of this fractional difference in the indices of refraction for this research was $\Delta \leq 0.01$. The physical effects of this small fractional difference are important to the modal analysis of step-index fibers.

As previously defined, the modes of an optical fiber satisfy Maxwell's equations and the appropriate boundary conditions. The boundary conditions are that the tangential components of the electric field (***E***) and magnetic field (***H***) are continuous at the interface of the core and cladding materials. The results of solving for the modes are eigenfunctions of the electric field with constant transverse distributions and polarizations throughout the fiber, which allow light, and hence information, to propagate down in the fiber. The modes also have distinct propagation constants, characteristic field distributions in the transverse plane and two independent states of polarization [3]. Although all types of fibers are parameterized by modal characteristics, the physical parameters of step-index fibers with $\Delta << 1$ allow closed-form solutions to Maxwell's equations and allow use of an approximation, the weakly-guiding approximation.

By noting that the fractional difference in the indices of refraction is small, use of the weakly-guiding approximation in solving for the modes of the optical fiber is permitted. The longitudinal components of the electric and magnetic fields are then much weaker than the transverse components and the guided waves are approximately transverse electromagnetic, or TEM [3]. This assumption that the modes of the fiber are nearly transverse allows use of the scalar wave approximation [3]. The modal fields of weakly guided fibers are found from Maxwell's equations to be waves propagating in the direction of the fiber axis, which we take to be the *z*-direction (see Fig. 2.1) [5]. The

states of polarization that the modes can have are in the *x*- and *y*-directions and these linear polarizations form orthogonal polarization states. The phenomenon of evanescent waves in the cladding that propagate in the *z*-direction but decay exponentially in the transverse direction is also present in the fiber. In non-weakly-guiding fibers, hybrid electric (*HE*), tranverse electric (*TE*) and transverse magnetic (*TM*) modes are present [6]. However, for weakly-guiding fibers, which are the type used for telecommunications, a superposition of the linearly polarized (*LP*) modes adequately describes the field in the fiber. Thus, the modes of interest for this thesis are the *LP* modes.

For the linearly polarized modes, the transverse component of the electric field, which will hereafter be denoted by Ψ, satisfies the scalar wave equation

$$\nabla^2\Psi = \frac{n^2}{c^2}\frac{\partial^2\Psi}{\partial t^2}, \tag{2.3}$$

where c is the speed of light in vaccuo and n is the index of refraction of the medium in question [2]. We now assume that the solution to Eq. (2.3) may be written in terms of cylindrical polar coordinates (r,ϕ, z) as

$$\Psi(r,\phi,z,t) = \psi(r,\phi)\cos\left(\beta z - \omega t\right), \tag{2.4}$$

where ω is the angular frequency of the light and β is the propagation constant of each mode. Substituting Eq. (2.4) into the wave equation, we obtain the following partial differential equation

$$\left[\frac{1}{r}\frac{\partial}{\partial r}\left(r\frac{\partial}{\partial r}\right) - \frac{1}{r^2}\frac{\partial^2}{\partial\phi^2}\right]\psi + \left(\frac{\omega^2}{c^2}n^2 - \beta^2\right)\psi = 0, \tag{2.5}$$

Application of the method of separation of variables to this equation leads to the following forms for the transverse field

$$\psi(r,\phi)=\begin{cases}\dfrac{A}{J_l(U)}J_l\left(\dfrac{U}{a}r\right)\begin{bmatrix}\cos l\phi\\ \sin l\phi\end{bmatrix}, & r<a\\ \dfrac{A}{K_l(W)}K_l\left(\dfrac{W}{a}r\right)\begin{bmatrix}\cos l\phi\\ \sin l\phi\end{bmatrix}, & r>a\end{cases}, \qquad l=0,1,\ldots, \tag{2.6}$$

where

$$U=a\left(k_0^2n_1^2-\beta^2\right)^{1/2}, \tag{2.7}$$

$$W=a\left(\beta^2-k_0^2n_2^2\right)^{1/2}, \tag{2.8}$$

$$k_0=\omega/c=2\pi/\lambda_0. \tag{2.9}$$

Here A is the amplitude of the wave, β can be determined from the knowledge of U and W, k_0 is the free space wave number and λ_0 is the wavelength of the light in vaccuo. In Eq. (2.6), $J_l(x)$ is the Bessel function of the first kind of order l and $K_l(x)$ is the modified Bessel function of the second kind of order l.

The Bessel functions give the transverse dependence of the modal field, which determines the distribution for a particular mode. The function $J_l(x)$ oscillates in a manner similar to sine or cosine functions, but with decaying amplitude as x increases. The function $K_l(x)$ decays exponentially with increasing x. The $\cos(\beta z-\omega t)$ term governs the propagation of the mode in the z-direction. The subscript l specifies the azimuthal dependence.

The constants U and W result from application of the separation of variables technique on Eq. (2.5). The transverse distribution of a given mode is influenced by U and W, because they are key variables in the argument of the Bessel and modified Bessel functions in Eq. (2.6). These parameters determine the rate of change of the mode in the core and the cladding, respectively. A large value of U means fasters oscillation of the radial distribution in the core. A large value of W means a faster decay and smaller penetration of the wave into the cladding [5].

The boundary conditions that the modes must satisfy are

$$\psi_{core}\big|_{r=a} = \psi_{cladding}\big|_{r=a} \tag{2.10}$$

$$\frac{\partial \psi_{core}}{\partial r}\Big|_{r=a} = \frac{\partial \psi_{cladding}}{\partial r}\Big|_{r=a}. \tag{2.11}$$

Substituting Eq. (2.6) into the boundary conditions results in a transcendental equation that must be solved,

$$U\frac{J_{l-1}(U)}{J_l(U)} = -W\frac{K_{l-1}(W)}{K_l(W)}. \tag{2.12}$$

Since U and W are related by

$$\left(U^2 + W^2\right)^{1/2} = \left(\frac{2\pi a}{\lambda_0}\right)\left(n_1^2 - n_2^2\right)^{1/2} \equiv V, \tag{2.13}$$

the transcendental equation can be solved for U as a function of V, the normalized waveguide parameter. W can then be obtained from Eq. (2.13).

For a given value of the azimuthal index, l, there are a finite number, $m = 1, 2, 3\ldots$, of solutions to the transcendental equation. The m^{th} solution is referred to as the LP_{lm} mode. The multiple solutions yield corresponding values of U and W, which

govern the spatial distributions in the core and in the cladding, respectively, and may be denoted U_{lm} and W_{lm} [5]. It can be shown that the subscripts l and m not only specify each mode but also provide information about the radial field distributions and intensity patterns for each mode. The number and location of zeros in the azimuthal and radial directions are dictated by l and m, respectively. In particular [2],

$$\text{number of } \phi \text{ direction zeros} = 2l \tag{2.14}$$

and

$$\text{number of radial direction zeros (not including } r = 0) = m - 1. \tag{2.15}$$

V is an important parameter in solving for the modes of an optical fiber. As seen in Eq. (2.13), the sum of the squares of U and W defines V. While many fiber parameters only describe either the fiber or electromagnetic wave properties, V depends on both the fiber parameters (n_1, n_2, and a) and the wavelength of the light [7]. Thus, many of the propagation characteristics, such as the number of modes, the propagation constant and the cutoff wavelength can be directly calculated by utilizing the normalized waveguide parameter.

Each mode has a cutoff value, denoted as V_c, which is the minimum allowed value of V. This occurs when $W = 0$ (see Eq. 2.13). The cutoff values are therefore specified by (see Eq. 2.12) the equations

$$J_{l-1}(V_c) = 0. \tag{2.16}$$

This illustrates the fact that V_c, and hence U_c, correspond to zeros of the Bessel functions, which is significant to the analytic approximation technique used in this thesis.

2.2 Analytic Approximation Technique

Solving the transcendental equation for the modes of an optical fiber can only be done numerically and can be computationally complicated. The literature provides alternative analytic approximation techniques whose results agree well with those of the numerical solution techniques [1,7-9]. For this thesis, we utilized the analytic approximation technique developed by Gloge [1]. This technique is based on the weakly-guiding approximation for step-index fibers, and in fact it initiated the use of the term "weakly-guiding fibers" [3,6]. Ghatak and Yariv support use of this approach as an accurate approximation for the modes and modal conditions in fibers used for telecommunication purposes, which require the weakly-guiding approximation condition for operation.

Through mathematical manipulation of Eq. (2.12), Gloge derived an analytic approximation equation for U as a function of V [1]. He found that, to a good approximation, that for $LP_{01,}$

$$U(V) = \frac{\left(1+\sqrt{2}\right)V}{\left[1+\left(4+V^4\right)^{1/2}\right]}, \tag{2.17}$$

and for all other modes

$$U(V) = U_c \exp\left[\frac{\arcsin\left(s/U_c\right) - \arcsin\left(s/V\right)}{s}\right], \tag{2.18}$$

where

$$s = \left(U_c^2 - l^2 - 1\right)^{\frac{1}{2}}. \tag{2.19}$$

In Eqs. (2.18) and (2.19) U_c is the m^{th} root of $J_{l-1}(U)$. Thus, U_c, obtained from a table of Bessel function zeros, and V, calculated from the fiber parameters, are used to determine the values of U and W for the mode. Using these values, expressions for the field, intensity and power distributions can be solved for numerically for parameter sets that correspond to weakly-guiding fibers.

In addition, the analytical expressions also allow the determination of the total possible number of modes in the fiber for a given V value. The number of modes M is therefore equal to the number of roots of $J_{l-1}(U)$ that are smaller than V [2]. For fibers that support a large number of modes, the total number of modes is approximately

$$M \approx \frac{V^2}{2}. \tag{2.20}$$

Since Eqs. (2.17) - (2.20) are simple equations that provide accuracy on the order of the square of fractional difference in indices of refraction [1], it was determined that the solutions this method provided were appropriate for this thesis.

2.3 Illustrations of Optical Fiber Modes Using MathCAD

MathCAD 8, a mathematical software package, was used to verify and illustrate the analytic approximation technique solutions for the modes of an optical fiber. The verification was done to develop a better understanding of the effectiveness of the approximation technique and graphical illustrations in preparation for calculation of the fractional guided power in each mode of the fiber. The symbols and ranges of inputs into the MathCAD worksheet are listed in Table 3.1.

Table 2.1 MathCAD Inputs with Symbols, Units and Ranges.

Input	**Symbol**	**Units/Dimensions**	**Range**
Amplitude	A	None	1
Core Index of Refraction	n_1	None	$1.45 \le n_1 \le 1.47$
Cladding Index of Refraction	n_2	None	$1.446 \le n_1$
Radius of the fiber	a	μm	$4 \le a \le 100$
Wavelength	λ	μm	$0.40 \le \lambda \le 1.60$
Order of eigenvalue equation	l	None	$l = 0 \,..\, 8$
m^{th} eigenfunction solution	m	None	$m = 1 \,..\, 19$

The normalized waveguide parameter, *V*, defined by Eq. (2.13) is calculated in the worksheet and used to determine *M* from a relational matrix as shown in Appendix A, an example MathCAD worksheet. $U_{c,lm}$, the cutoff value for a particular mode, is selected, from a table of the Bessel functions roots using subscripts *l* and *m* from user inputs. $U_{c,lm}$ is used with Eq. (2.18) to calculate the value of *U* for the given mode, which is combined with *V* to determine *W*. The values of *W* and *U* are input into MathCAD equations equivalent to Eq. (2.6) to plot the field and the intensity. Although, the electric field can not be observed, intensity, calculated in $I = |\psi|^2$, is observable and measurable. It is, therefore, a key quantity in this thesis. The field and the intensity are plotted in Cartesian coordinates based on the radius of the fiber input initially into each worksheet. The equation is used to incrementally step through the fiber, solving for the field and intensity

at each position. The results are plots of the field and the intensity as functions of *x* and *y*, as seen in Figs. 2.2 and 2.3 below.

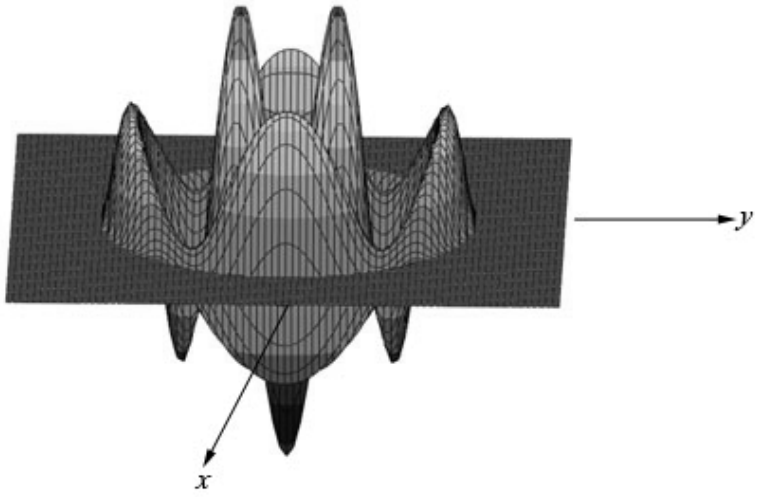

Figure 2.2 MathCAD plot of LP_{23} field distribution.

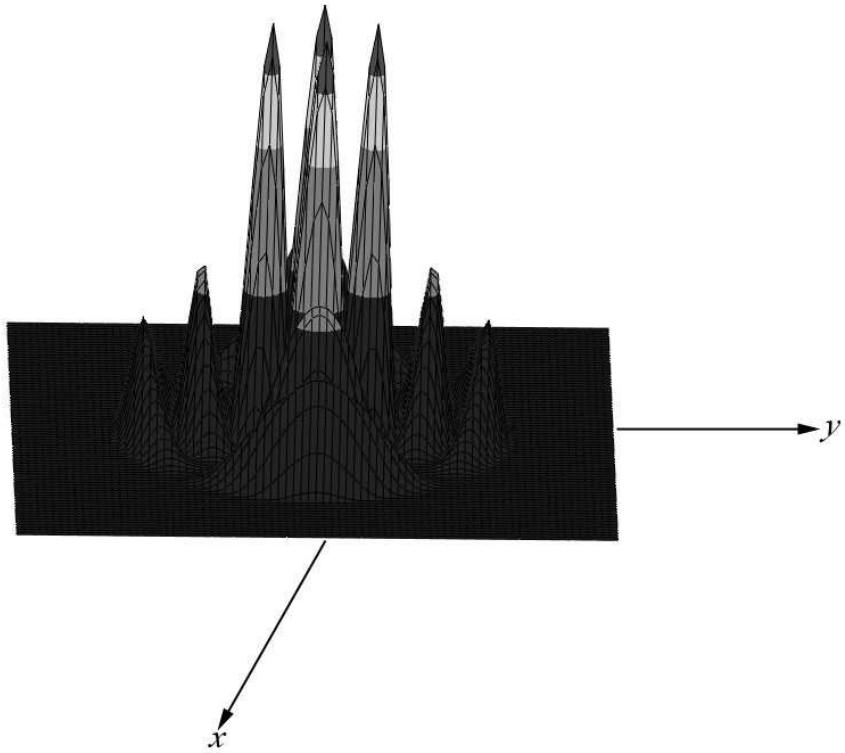

Figure 2.3 MathCAD plot of LP_{23} intensity distribution.

2.4 Concluding Remarks

In this chapter the basic theory of the modes of a step-index fiber was presented, and an analytical approximation technique, valid for weakly-guiding fibers, was described. The analytic approximation method:

- provides results that are accurate compared with the results from the numerical technique,
- provides a straightforward, simple method to solve for various eigenvalues by changing the parameters in the equations that result from the method.

Therefore, the Gloge analytic approximation technique was chosen to be used as the basis for this thesis.

CHAPTER III

EVALUATION OF FRACTIONAL POWER IN A LARGE DIAMETER OPTICAL FIBER

In the last chapter, the basic concepts regarding the modes of an optical fiber were introduced. In this chapter, we investigate theoretically the effect of varying the angle of incidence on the fractional guided power per mode and the total fractional power transmitted by an optical fiber of large radius. From previous studies, we see that the amount of light transmitted along the fiber is found by summing the power transmitted in each mode and that it is of interest to consider the contributions of the individual modes to the total light power transmitted in the fiber [11]. Since we are only concerned with the light guided in the fiber, the light that is radiated from the fiber is not considered in this analysis.

For this thesis in particular, the numerical values used will be those of the fiber in the experiment of Chapter IV, which had a radius of 100μm, in order to compare the theoretical and experimental results. This large optical fiber has large values for V and W, which lead to asymptotic behavior in the modal field that is accounted for in this chapter. In the experiment, the optical fiber is excited by a Gaussian beam whose angle of incidence with respect to the axis of the fiber is varied by small amounts as illustrated in

Fig. 3.1. Based on these modal and experimental parameters, a new expression for the power per mode for large fibers is developed in section 3.1.3. Results from application of this theory to the 100μm fiber show that each l = 0 mode exhibits a peak in fractional power at normal incidence and that the higher order modes l = 1 and l = 2 peak at other angles and have minimal fractional power when $\theta_i = 0$.

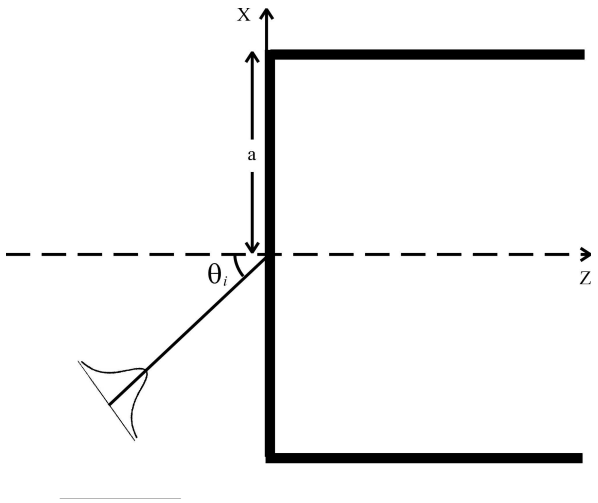

Figure 3.1 Illustration of Gaussian beam entering a large diameter optical fiber at angle of incidence, θ_i.

3.1 Determining the power ratio, P_l / P_i, in each mode

The literature provides general expressions for the ratio of the guided power in each mode to the incident power, denoted P_l / P_i, which are used to calculate the fiber output power in this thesis. When the incident field is a Gaussian beam of spot size ρ_s traveling in a medium of index of refraction n_i, the expression for the incident power is

$$P_i = \frac{\pi}{2}\left(\frac{\varepsilon_o}{\mu_o}\right)^{1/2} n_i \rho_s , \qquad (3.1)$$

where ε_0 and μ_0 are respectively, the permittivity and permeability of free space. The equation for the power in each mode, P_l, for fibers with a circular cross section is given by [4]

$$P_l = \frac{a^2 n_1}{4\pi}\left(\frac{\varepsilon_0}{\mu_0}\right)^{\frac{1}{2}} \frac{|\alpha_l|^2}{N_l}, \tag{3.2}$$

where

$$\alpha_l = \int_0^{\infty}\int_0^{2\pi} E_x(aR)\psi_l(R,\phi)\,RdRd\phi, \tag{3.3}$$

$$N_l = \int_0^{\infty} F_l^{\,2}(R)\,RdR, \tag{3.4}$$

and $E_x(aR)$ is the amplitude of the incident electric field. In our case the incident field is that of a Gaussian beam,

$$E_x(aR) = f(aR)\exp\{ikn_i(\theta_i aR\cos\phi + z\}, \tag{3.5}$$

where

$$f(aR) = \exp\left\{-\frac{1}{2}\left(\frac{a}{\rho_s}R\right)^2\right\} \tag{3.6}$$

is the amplitude distribution of the beam. The $\psi_l(R,\phi)$ term in Eq. (3.3) represents the modal field distributions discussed in Chapter II

$$\psi_l(R,\phi) = F_l(R)\begin{cases}\cos(l\phi)\\ \sin(l\phi)\end{cases}, \tag{3.7}$$

where

$$F_l(R)=\begin{cases}\dfrac{J_l(UR)}{J_l(U)}, & 0\le R\le 1\\ \dfrac{K_l(WR)}{K_l(W)}, & 1<R<\infty\end{cases}. \tag{3.8}$$

Here $R=r/a$ is the normalized fiber radius. In this thesis the incident field is taken to be a Gaussian beam, because this corresponds to the incident field used in the experiments of Chapter IV, which used the field from a laser oscillating in its TEM_{00} mode.

We begin evaluating α_l by substituting Eqs. (3.5) and (3.7) into Eq. (3.3),

$$\begin{aligned}\alpha_l &= \int_0^{\infty}\int_0^{2\pi} f(aR)\exp\left[ikn_i(\theta_i aR\cos\phi+z)\right]F_l(R)\begin{bmatrix}\cos(l\phi)\\ \sin(l\phi)\end{bmatrix}RdRd\phi,\\ &= \exp(ikn_i z)\int_0^{\infty} f(aR)F_l(R)\begin{bmatrix}B_l^{(1)}(\kappa R)\\ B_l^{(2)}(\kappa R)\end{bmatrix}RdR,\end{aligned} \tag{3.9}$$

where

$$\begin{aligned}B_l^{(1)}(\kappa R)&=\int_0^{2\pi}\exp(i\kappa R\cos\phi)\cos(l\phi)\,d\phi, \quad (l=0,1,\ldots),\\ B_l^{(2)}(\kappa R)&=\int_0^{2\pi}\exp(i\kappa R\cos\phi)\sin(l\phi)\,d\phi, \quad (l=1,2,\ldots),\end{aligned} \tag{3.10}$$

and $\kappa=ak_0n_i\theta_i$. Here k_0 is the free space wave number and θ_i is the angle of incidence of the beam with respect to the fiber axis. κ is a function of the angle of incidence θ_i, but this dependence will not be shown explicitly for notational convenience. κ is the variable in the expression for the power ratio that determines the angular dependence of the output power on the angle of incidence.

To account for the excitation of all the modes by a tilted Gaussian beam, the well-known identity

$$\exp\left(i\kappa R\cos\phi\right) = J_0\left(\kappa R\right) + 2\sum_{p=1}^{\infty} i^p J_p\left(\kappa R\right)\cos p\phi \tag{3.11}$$

is substituted into Eqs. (3.10a) and (3.10b). It follows that

$$B_l^{(1)}\left(\kappa R\right) = J_0\left(\kappa R\right)\int_0^{2\pi}\cos\left(l\phi\right)d\phi + 2\sum_{p=1}^{\infty} i^p J_p\left(\kappa R\right)\int_0^{2\pi}\cos\left(p\phi\right)\cos\left(l\phi\right)d\phi \tag{3.12}$$

$$B_l^{(2)}\left(\kappa R\right) = J_0\left(\kappa R\right)\int_0^{2\pi}\sin\left(l\phi\right)d\phi + 2\sum_{p=1}^{\infty} i^p J_p\left(\kappa R\right)\int_0^{2\pi}\sin\left(p\phi\right)\cos\left(l\phi\right)d\phi\,. \tag{3.13}$$

It is shown in Appendix B that Eqs. (3.12) and (3.13) simplify to

$$B_l^{(1)}\left(\kappa R\right) = 2\pi i^l J_l\left(\kappa R\right), \quad l = 0,1,\ldots \tag{3.14a}$$

$$B_l^{(2)}\left(\kappa R\right) = 0, l = 0,1,\ldots\,. \tag{3.14b}$$

Thus, only the $\cos\left(l\phi\right)$ term effects α_l and Eq. (3.3) becomes

$$\alpha_l = 2\pi i^l\int_0^{\infty} f\left(aR\right)F_l\left(R\right)J_l\left(\kappa R\right)R\,dR, \quad l = 0,1,\ldots\,. \tag{3.15}$$

Inserting Eq. (3.8) into Eq. (3.9) yields

$$\alpha_l = 2\pi i^l\left[I_l^{(1)} + I_l^{(2)}\right] \tag{3.16}$$

where

$$I_l^{(1)} = \int_0^1 \frac{f\left(aR\right)J_l\left(UR\right)J_l\left(\kappa R\right)}{J_l\left(U\right)}RdR\,, \tag{3.17}$$

$$I_l^{(2)} = \int_1^{\infty} \frac{f\left(aR\right)K_l\left(WR\right)J_l\left(\kappa R\right)}{K_l\left(W\right)}RdR\,. \tag{3.18}$$

The two integrals, $I_l^{(1)}$ and $I_l^{(2)}$, correspond, respectively, to the power in the core and cladding.

To determine evaluation methods for the integrals that will allow comparison with the experiments, we must consider the fiber and modal parameters of the experimental fiber, which are listed in Table 3.1. The *V* value of this fiber was calculated from Eq. (2.13) and is equal to 298.6, which is extremely large. This is due to the large core radius of the fiber (100μm) and the relatively short wavelength (632.8nm) of the incident light. The corresponding *W* values are approximately 300. Based on the experimental range of angles, $\theta_i = 0..18^o$, the values for κ, which depends on the incident angle, θ_i, also assumes large values as the angle increases. Note that the *U* values were not found to be large compared to *V* and *W* for any modes of the modes for this thesis.

Table 3.1 Experimental Inputs with Symbols, Units and Values.

Parameter	**Symbol**	**Units/Dimensions**	**Value/Range**
Amplitude	A	None	1
Core Index of Refraction [8]	n_1	None	1.474
Cladding Index of Refraction	n_2	None	1.443
Index of Refraction of Source Medium	n_i	None	1
Spot Size of He Ne Laser	ρ_s	μm	5
Radius of the fiber [8]	a	μm	100
Wavelength of He-Ne Laser	λ	μm	0.6328
Normalized Waveguide Frequency	V	None	298.6
Angular Dependence of the Incident Beam	κ	None	0 - 312

The spot size of the incident beam was too small to be measured with the apparatus that was available. For the purposes of this thesis, the spot size was estimated to be 5μm.

In Chapter II, we mentioned that large *W* values indicate faster decay of the evanescent wave and a smaller penetration of the wave into the cladding [5] due to the asymptotic (i.e. large argument) behavior of $K_l(x)$. The function decreases exponentially to zero for large values of its argument. In addition to *W* causing asymptotic behavior, κ also causes asymptotic behavior in Eqs. (3.17) and (3.18) for values $\kappa >> 1$. To derive expressions for these integrals, the asymptotic forms of the $J_l(x)$ and $K_l(x)$ will be utilized. The asymptotic forms of these functions, valid for $x >> 1$, are

$$J_l(x) \approx \left(\frac{2}{\pi x}\right)^{1/2} \cos\left[x - \left(l + \frac{1}{2}\right)\frac{\pi}{2}\right], \tag{3.19}$$

$$K_l(x) \approx \left(\frac{\pi}{2x}\right)^{1/2} e^{-x}. \tag{3.20}$$

Use of the asymptotic forms in Eqs. (3.17) and (3.18) will allow us to evaluate and compare the values of the core and cladding integrals. Due to the large values of *W* and κ, and the resulting asymptotic behavior of the $J_l(x)$ and $K_l(x)$, the cladding integral is expected to be negligibly small compared to the core integral. Upon determining which integrals have significant values, the result will be the final expression to calculate the power in each mode.

To account for $\kappa >> 1$ values, the core and cladding integrals will be split into non-asymptotic and asymptotic regions for the κ values of interest. Since the integration is over the normalized fiber radius, *R*, which is in the argument of $J_l(\kappa R)$, the *R* value, call

it $\bar{R}_l$, at which the asymptotic behavior begins is a key quantity. Let x_l be the value of the argument of $J_l(x)$ that specifies the beginning of asymptotic behavior. $\bar{R}_l$ is then defined by means of $\kappa\bar{R}_l = x_l$.

When $\bar{R}_l < 1$, Eq. (3.17) is divided into an initial part integrated from zero to $\bar{R}_l$, where $J_l(x)$ does not behave asymptotically, and a subsequent part integrated from $\bar{R}_l$ to 1, where $J_l(x)$ behaves asymptotically. For $\bar{R}_l > 1$, Eq. (3.18) is divided into a section integrated from 1 to $\bar{R}_l$ where $J_l(x)$ does not behaving asymptotically and a subsequent section integrating from $\bar{R}_l$ to infinity where $J_l(x)$ behaves asymptotically.

3.1.1 Evaluation for α_l when $\bar{R}_l < 1$

In this case, Eq. (3.17) can be divided into non-asymptotic and asymptotic parts. Inserting Eq. (3.19), the asymptotic expansion for $J_l(x)$, into Eq. (3.17) leads to the following expression,

$$I_l^{(1)} = \frac{1}{J_l(U)}\left\{\int_0^{\bar{R}_l} \exp\left(-\gamma^2 R^2\right) J_l(UR)\, J_l(\kappa R)\, R dR + \sqrt{\frac{2}{\pi\kappa}}\int_{\bar{R}_l}^{1} \exp\left(-\gamma^2 R^2\right)\cos\left[\kappa R - \frac{\pi}{2}\left(l+\frac{1}{2}\right)\right]\sqrt{R}\, dR\right\} \tag{3.21}$$

where $\gamma = a/\sqrt{2}\rho_s$. It therefore follows that α_l takes the following form when $\bar{R}_l < 1$

$$\alpha_l = 2\pi i^l \left(\frac{1}{J_l(U)} \left\{ \int_0^{\bar{R}_l} \exp\left(-\gamma^2 R^2\right) J_l(UR) J_l(\kappa R) R dR + \sqrt{\frac{2}{\pi\kappa}} \int_{\bar{R}_l}^{1} \exp\left(-\gamma^2 R^2\right) \cos\left[\kappa R - \frac{\pi}{2}\left(l + \frac{1}{2} \right) \right] \sqrt{R} dR \right\} + I_l^{(2)} \right) .$$

(3.22)

It is shown in Appendix C that for $\bar{R}_l < 1$ the asymptotic approximation of $I_l^{(2)}$ is

$$I_l^{(2)} = C_1 \left\{ \frac{\exp\left[-\left(\frac{W^4}{4\gamma^2} - q_1 W^2 - W \right) \right]}{\Omega_1(W)} \cos\left[\Lambda_1(W) + \left(l + \frac{1}{2} \right) \frac{\pi}{2} \right] \right\}, \tag{3.23}$$

where

$$q_1 = \frac{3}{2} + \frac{\kappa^2}{\gamma^2} - \frac{3}{4} \tag{3.24}$$

$$C_1 = \frac{1}{2\pi\gamma^2} \sqrt{\frac{2}{\kappa}} \exp\left[\sigma_1 \kappa^2 - \frac{\kappa^4}{4\gamma^2} + \gamma^2 \right], \tag{3.25}$$

$$\sigma_1 = -\frac{1}{4} + \gamma^2 , \tag{3.26}$$

$$\Omega_1(W) = 1 + \frac{W^2}{2\gamma^2} - \frac{\kappa^2}{2\gamma^2} , \tag{3.27}$$

$$\Lambda_1(W) = \frac{\kappa W^3}{\gamma^2} - \frac{\kappa^3 W}{4\gamma^4} - \frac{3}{2}\kappa W . \tag{3.28}$$

For the parameter ranges of interest, $W \approx 300$ and $\gamma \approx 40$, the term $\exp\left(-W^4/4\gamma^4\right)$ in Eq. (3.23) is extremely small. This makes $I_l^{(2)}$ negligibly small compared to the first two

terms in Eq. (3.22); therefore, it is omitted from here on. As a result, the following equation provides the final expression for α_l when $\bar{R}_l < 1$,

$$\alpha_l = 2\pi i^l \left\{ \frac{1}{J_l(U)} \left[\int_0^{\bar{R}_l} \exp\left(-\gamma^2 R^2\right) J_l(UR)\, J_l(\kappa R)\, R dR + \sqrt{\frac{2}{\pi\kappa}} \int_{\bar{R}_l}^{1} \exp\left(-\gamma^2 R^2\right) \cos\left[\kappa R - \frac{\pi}{2}\left(l + \frac{1}{2}\right)\right] \sqrt{R} dR \right] \right\}. \tag{3.29}$$

3.1.2 Evaluation of α_l when $\bar{R}_l \geq 1$

For this case, $I_l^{(1)}$ can be evaluated without splitting the integral because its lower limit of integration occurs at $R = 1$. Therefore, we now investigate the evaluation of $I_l^{(2)}$. The cladding integral, Eq. (3.18), will be divided into non-asymptotic and asymptotic parts, where asymptotic behavior occurs when $\kappa \bar{R}_l \geq x_l$. Inserting the asymptotic expansion for $J_l(x)$ into Eq. (3.18) leads to the following division of the cladding integral

$$I_l^{(2)} = \frac{1}{K_l(W)} \left\{ \int_1^{\bar{R}_l} \exp\left(-\gamma^2 R^2\right) K_l(WR)\, J_l(\kappa R)\, R dR + \sqrt{\frac{2}{\pi\kappa}} \int_{\bar{R}_l}^{\infty} \exp\left(-\gamma^2 R^2\right) K_l(WR) \cos\left[\kappa R - \frac{\pi}{2}\left(l + \frac{1}{2}\right)\right] \sqrt{R} dR \right\}. \tag{3.30}$$

Since $W \approx 300$, the use of the asymptotic form $K_l(WR)$ gives the result

$$I_l^{(2)} = I_l^{(3)} + I_l^{(4)}, \tag{3.31}$$

where

$$I_l^{(3)} = \int_1^{\bar{R}_l} g(R) J_l(\kappa R)\sqrt{R}\,dR\,, \tag{3.32}$$

$$I_l^{(4)} = \sqrt{\frac{2}{\pi\kappa}} \int_{\bar{R}_l}^{\infty} g(R)\cos\left[\kappa R - \frac{\pi}{2}\left(l+\frac{1}{2}\right)\right] dR\,, \tag{3.33}$$

$$g(R) = \exp\left[-\gamma^2 R^2 - W(R-1)\right]. \tag{3.34}$$

$I_l^{(3)}$ can not be evaluated analytically, so an approximate upper bound expression will be used to estimate its value. It is shown in Appendix D that

$$\left|I_l^{(3)}\right| \le \left|\frac{\sqrt{\bar{R}_l}}{\gamma}\left\{\frac{1}{\left(1+\frac{W}{2\gamma^2}\right)\exp\left(\gamma^2\right)} - \frac{1}{\left(\bar{R}_l+\frac{W}{2\gamma^2}\right)\exp\left(\gamma^2\bar{R}_l^2\right)\exp(sW)}\right\}\right|, \tag{3.35}$$

gives $\exp(sW) = \exp\left[W\left(\bar{R}_l - 1\right)\right]$ and, since $\bar{R}_l \ge 1$, s is a real positive number. For parameter ranges of interest, $W \approx 300$ and $\gamma \approx 40$. It, therefore, follows that both terms in brackets in Eq. (3.35) are extremely small. This makes $\left|I_l^{(3)}\right|$ negligibly small compared to $I_l^{(1)}$. Thus, $I_l^{(3)}$ will not be included in the expression for α_l for $\bar{R}_l \ge 1$.

The next step is to solve for an approximate expression for $I_l^{(4)}$ in Eq. (3.33). It is shown in Appendix E that

$$I_l^{(4)} = C_2 \frac{\exp\left[-\left(\frac{W^4}{4\gamma^2} - q_2 W^2 - W - \eta\bar{R}_l\right)\right]}{\Omega_2(W)} \cos\left[\Lambda_2(W) + \left(l+\frac{1}{2}\right)\frac{\pi}{2}\right], \tag{3.36}$$

where

$$q_2 = \frac{1}{4} + \frac{3\kappa^2}{2\gamma^2} - \bar{R}_l, \tag{3.37}$$

$$\eta = \gamma^2 \bar{R}_l - \kappa^2, \tag{3.38}$$

$$C_2 = \frac{1}{2\gamma^2}\sqrt{\frac{2}{\pi\kappa}}, \tag{3.39}$$

$$\Omega_2(W) = \bar{R}_l + \frac{W^2}{2\gamma^2}, \tag{3.40}$$

$$\Lambda_2(W) = \frac{\kappa W^3}{\gamma^2} - \frac{\kappa^2 W}{4\gamma^2} - \left(\frac{1}{2} + \bar{R}_l\right)\kappa W. \tag{3.41}$$

For the parameter ranges of interest, $W \approx 300$ and $\gamma \approx 40$, and the term $\exp\left(-W^4/4\gamma^2\right)$ is extremely small. This makes the $I_l^{(4)}$ negligibly small compared to $I_l^{(1)}$. Therefore, $I_l^{(4)}$ will not be included in the evaluation of α_l for $\bar{R}_l > 1$. As a result the following equation provides the final expression for α_l when $\bar{R}_l > 1$,

$$\alpha_l = 2\pi i^l \int_0^1 \frac{\exp\left(-\gamma^2 R^2\right) J_l(UR) J_l(\kappa R)}{J_l(U)} R dR. \tag{3.42}$$

3.1.3 Final Expression for P_l / P_i

The general expression for α_l can be written as

$$\alpha_l = \frac{2\pi i^l}{J_l(U)} \begin{cases} \displaystyle\int_0^{\bar{R}_l} \exp\left(-\gamma^2 R^2\right) J_l(\kappa R)\, RdR + \sqrt{\frac{2}{\pi\kappa}} \int_0^{\bar{R}_l} J_l(UR) \cos\left[\kappa R - \left(l+\frac{1}{2}\right)\frac{\pi}{2}\right] \sqrt{R}\, dR, & \bar{R}_l < 1 \\ \displaystyle\int_0^1 \exp\left(-\gamma^2 R^2\right) J_l(UR)\, J_l(\kappa R)\, RdR, & \bar{R}_l \geq 1 \end{cases} .$$

(3.43)

To obtain a complete expression for P_l, the power in each mode, we need to include N_l from Eq. (3.4). It is well-known [4] that

$$N_l = \frac{V^2}{2U^2} \frac{K_{l-1}(W) K_{l+1}(W)}{K_l^2(W)} . \tag{3.44}$$

Since W is large in our work, we use the asymptotic expression for each $K_l(W)$ term in Eq. (3.44). It then follows that

$$N_l = \frac{V^2}{2U^2} . \tag{3.45}$$

Inserting Eqs. (3.43) and (3.45) into Eq. (3.2) gives the expression for the power in each mode as

$$P_l = 2\pi n_1 a^2 \left(\frac{U}{V}\right)^2 \left| \frac{1}{J_l(U)} \begin{cases} \displaystyle\int_0^{\bar{R}_l} \exp\left(-\gamma^2 R^2\right) J_l(\kappa R)\, RdR + \\ \qquad \displaystyle\sqrt{\frac{2}{\pi\kappa}} \int_0^{\bar{R}_l} J_l(UR) \cos\left[\kappa R - \left(l+\frac{1}{2}\right)\frac{\pi}{2}\right] \sqrt{R}\, dR, & \bar{R}_l < 1 \\ \displaystyle\int_0^1 \exp\left(-\gamma^2 \bar{R}^2\right) J_l(UR)\, J_l(\kappa R)\, RdR, & \bar{R}_l \geq 1 \end{cases} \right|^2 .$$

(3.46)

In order to evaluate the power ratio in each mode, Eq. (3.46) is divided by Eq. (3.1) and we find that the fractional power per mode is

$$\frac{P_l}{P_i}=4n_1\left(\frac{aU}{\rho_s V}\right)^2\left|\frac{1}{J_l(U)}\begin{cases}\displaystyle\int_0^{\bar{R}_l}\exp\left(-\gamma^2R^2\right)J_l(\kappa R)RdR+ & \\ \qquad\displaystyle\sqrt{\frac{2}{\pi\kappa}}\int_{\bar{R}_l}^{1}J_l(UR)\cos\left[\kappa R-\left(l+\frac{1}{2}\right)\frac{\pi}{2}\right]\sqrt{R}dR, & \bar{R}_l<1\\ \displaystyle\int_0^{1}\exp\left(-\gamma^2R^2\right)J_l(UR)J_l(\kappa R)RdR, & \bar{R}_l\geq 1\end{cases}\right|^2. \tag{3.47}$$

3.2 Theoretical Analysis and Results

In order to evaluate the fractional power per mode with Eq. (3.47), we note that both P_l and $\bar{R}_l$ depend on *l*. Therefore, changes in the values of $\bar{R}_l$ and the expression for P_l are necessary for specific orders. As indicated earlier, $\bar{R}_l = x_l/\kappa$, where κ is linearly dependant on θ_i, so hereafter it will be denoted as $\kappa(\theta_i)$. For each order, $\bar{R}_l$ is determined by dividing x_l by the smallest $\kappa(\theta_i)$ that causes $\bar{R}_l<1$. These values for $\bar{R}_l$ are found in Table 3.2. For P_l, Eq. (3.47) is a piecewise function in MathCAD (see Appendix A) that evaluates the power ratio for $\bar{R}_l<1$ and $\bar{R}_l>1$ for the $\bar{R}_l$ values in Table 3.2. These steps ensure that correct power calculations are being performed for each order, and hence for each mode.

Table 3.2 Asymptotic argument, x_l, and $\bar{R}_l$ for modes of various orders.

l	x_l	$\bar{R}_l$
0-1	10	10/17.33 = 0.577
2-3	20	20/25.99 = 0.769
4-8	60	60/60.65 = 0.989

To calculate numerical values for the fractional power per mode in each LP_{lm} mode, Eq. (3.47) is evaluated in the MathCAD worksheets used in Chapter II to illustrate the field and intensity distributions. Using Eq. (2.20) with V = 298.6 gives 44,580 as an approximation for the total number of modes in the experimental fiber. Calculation of the fractional guided power per mode was performed for modes with index values l = 0,1..8 and m = 1,2..19, which are the initial 171 modes of the approximation. For this thesis, the fractional power calculations are limited to those 171 modes for the following reasons:

- The standard tables have Bessel function zeros for l = 0-8 and m = 1-20 only.
- MathCAD has limited programming and matrix capabilities that prevent the use of large amounts of numerical values calculated and stored simultaneously.

The modes and U values for which the fractional power was calculated are listed in Appendix F.

The fractional power per LP_{lm} mode is calculated using Eq. (3.47) in which the m index is suppressed. Hereafter, it will not be suppressed and the fractional power per mode, P_l / P_t, will be denoted as, $\mathcal{P}_{lm}$. We also differentiate $\mathcal{P}_{lm}$ from the fractional power per order, $\mathcal{P}_l$, and the total fractional power in the fiber, $\mathcal{P}$, which are defined by

$$\mathcal{P}_l = \sum_{m=1}^{19} \mathcal{P}_{lm}, \quad \text{for } l = 0..8, \tag{3.48}$$

$$\mathcal{P} = \sum_{l=0}^{8} \mathcal{P}_l \, . \tag{3.49}$$

The calculations of the power per mode and power per order provide detailed information about the distribution of power in the 171 modes of the fiber that were investigated in this thesis. The results are graphically illustrated in Figs. 3.2-3.10.

3.2.1 Fractional Power in the l = 0 modes

The fractional power in the $l = 0$, $m = 1$ (LP_{01}) mode is plotted as a function of the angle of incidence, θ_i, in Fig. 3.2. This plot tells us that the power peaks at normal incidence $(\theta_i = 0)$ and that at normal incidence one-half the incident power is in the LP_{01} mode. Figs. 3.3 and 3.4 show plots of the fractional power in the $l = 0$ modes with larger *m* values, $m = 2,3,5\ldots19$. The fractional power in each mode increases until LP_{07} and then monotonically decreases as a function of *m*. These curves also peak at normal incidence until LP_{013}. For LP_{013} and higher, each curve has a trough at normal incidence and peaks at two angles symmetrically positioned with respect to $\theta_i = 0$. The fractional power in each mode with a trough also monotonically decreases as a function of *m*. Note the difference in scale between Fig. 3.2 and Figs. 3.3 and 3.4; the higher *m* modes transmit an order of magnitude less power as compared to the LP_{01} mode.

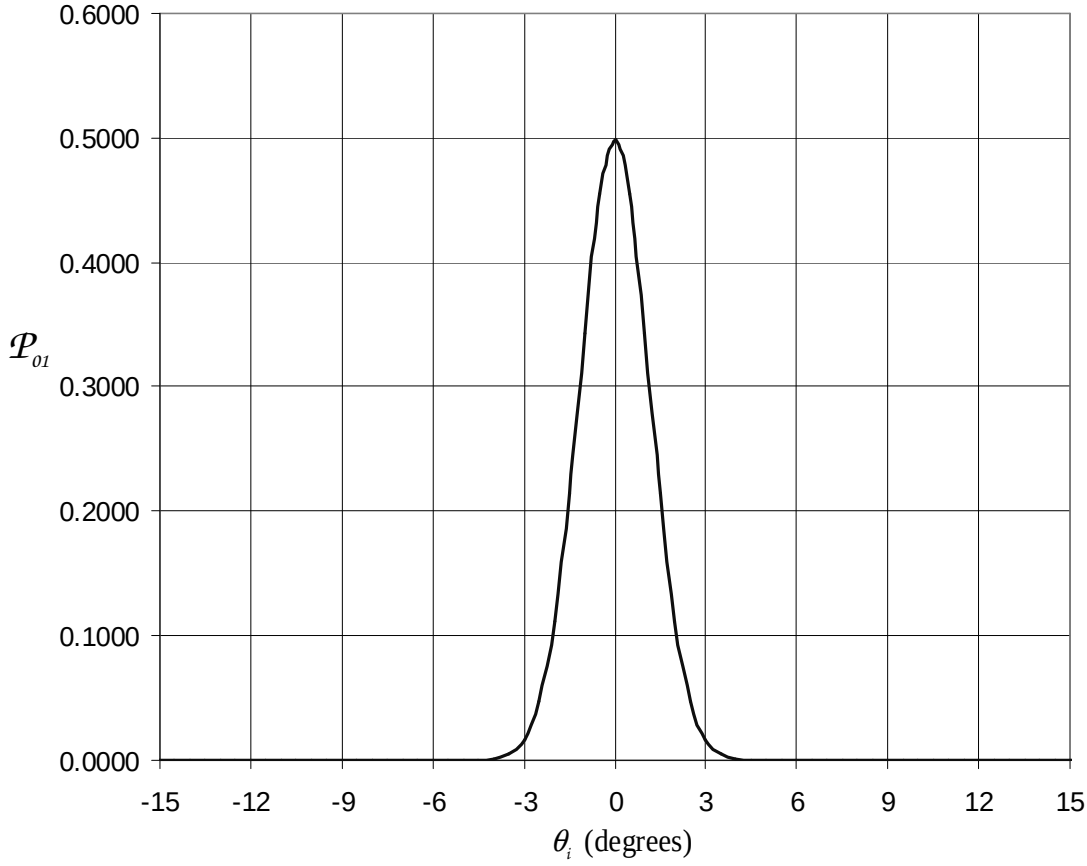

Figure 3.2 Fractional power for LP_{01} as a function of the angle of incidence.

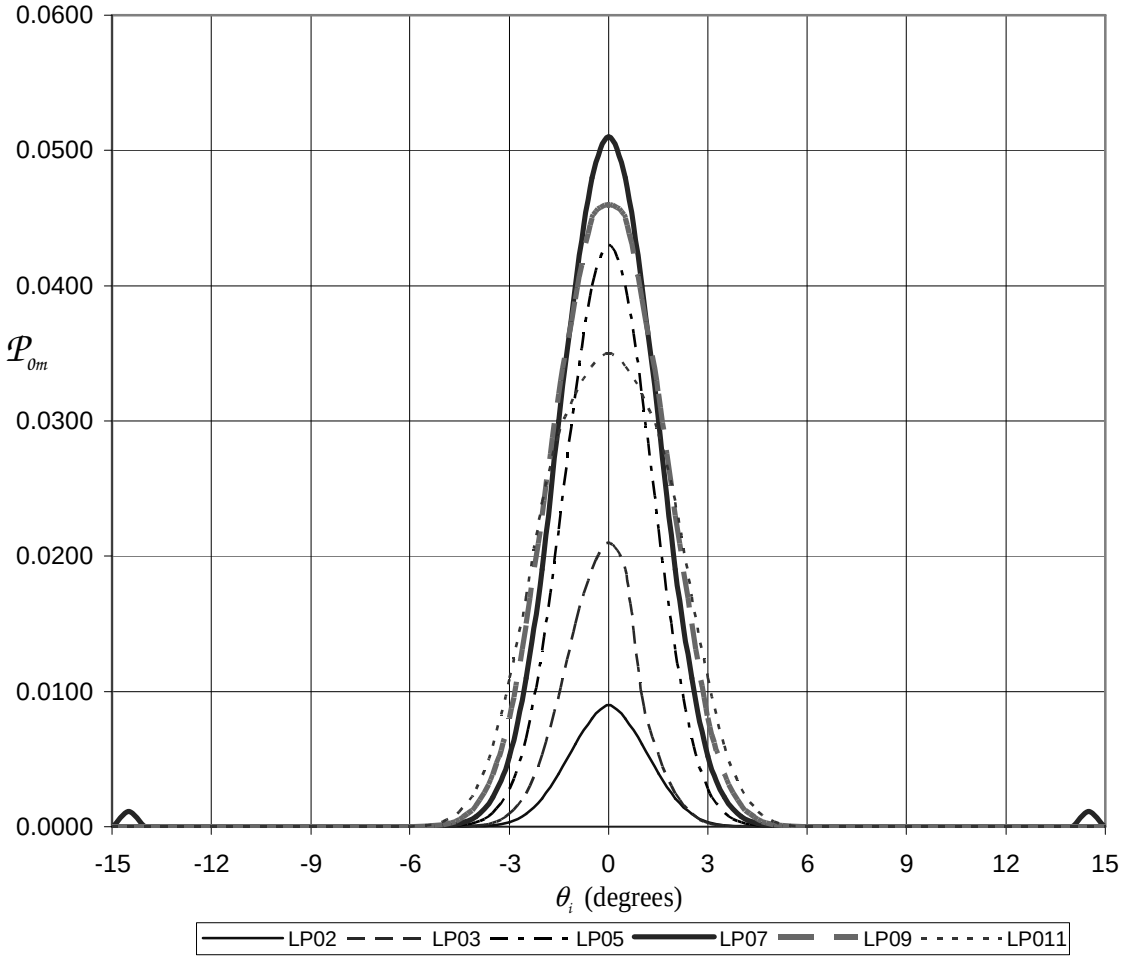

Figure 3.3 Fractional power for $l = 0$, $m = 2, 3, 5, 7, 9, 11$ modes as a function of the angle of incidence.

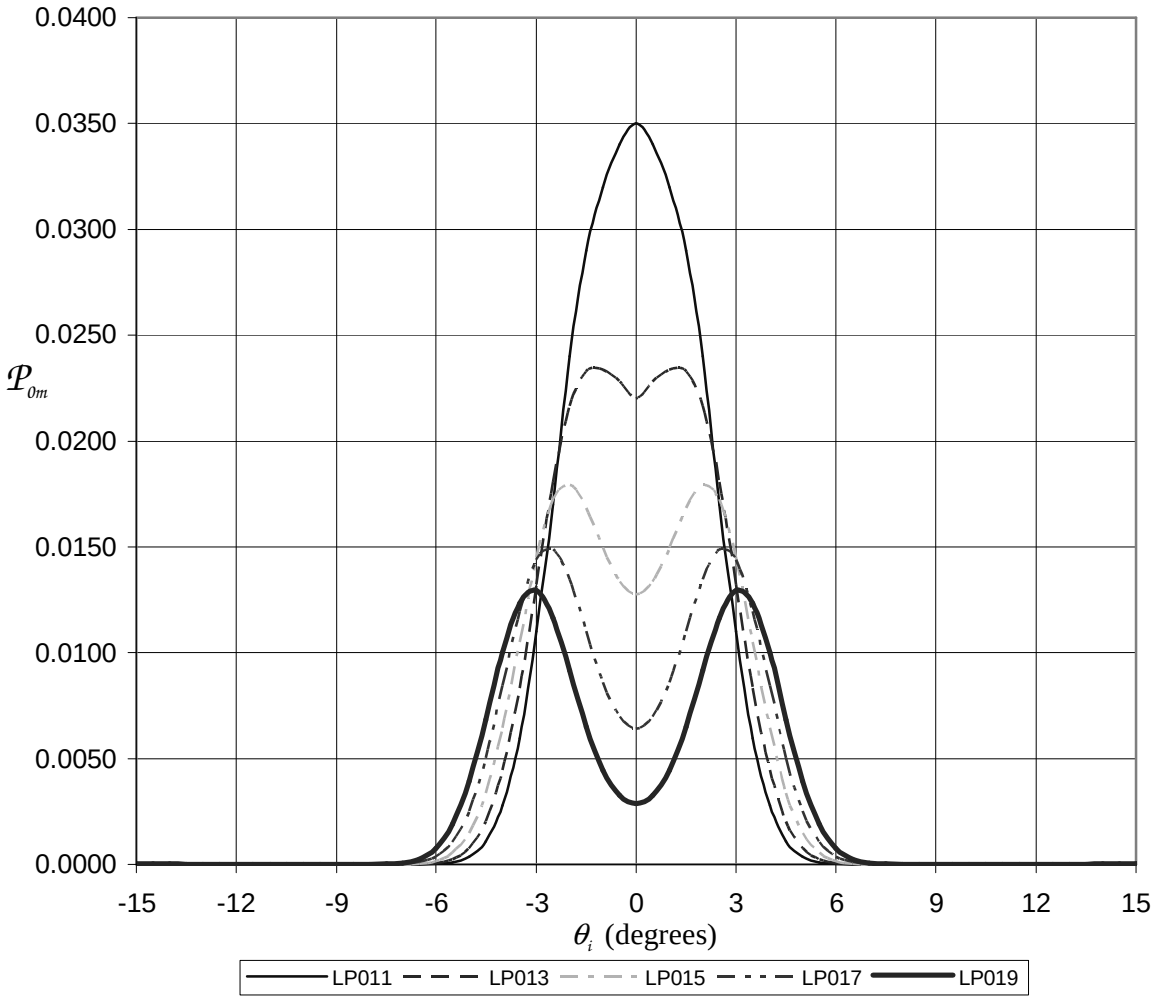

Figure 3.4 Fractional power for l = 0, m = 11, 13, 15, 17, 19 modes as a function of the angle of incidence.

3.2.2 Fractional Power in Higher Order Modes $(l > 0)$

The fractional power per mode for various $l = 1$, 2, 5 and 8 modes is plotted as a function of the angle of incidence, θ_i, in Figs. 3.5-3.9. These curves show us that for normal incidence each higher order mode exhibits a trough with minimum power values of zero, suggesting no fractional power in each mode when $\theta_i = 0$. Fig. 3.5 plots the

fractional power in the LP_{12} and LP_{23} modes. These are the lowest order modes for l = 1 and l = 2 that have significant amounts of power; the power in the LP_{11}, LP_{21} and LP_{22} modes is very small.

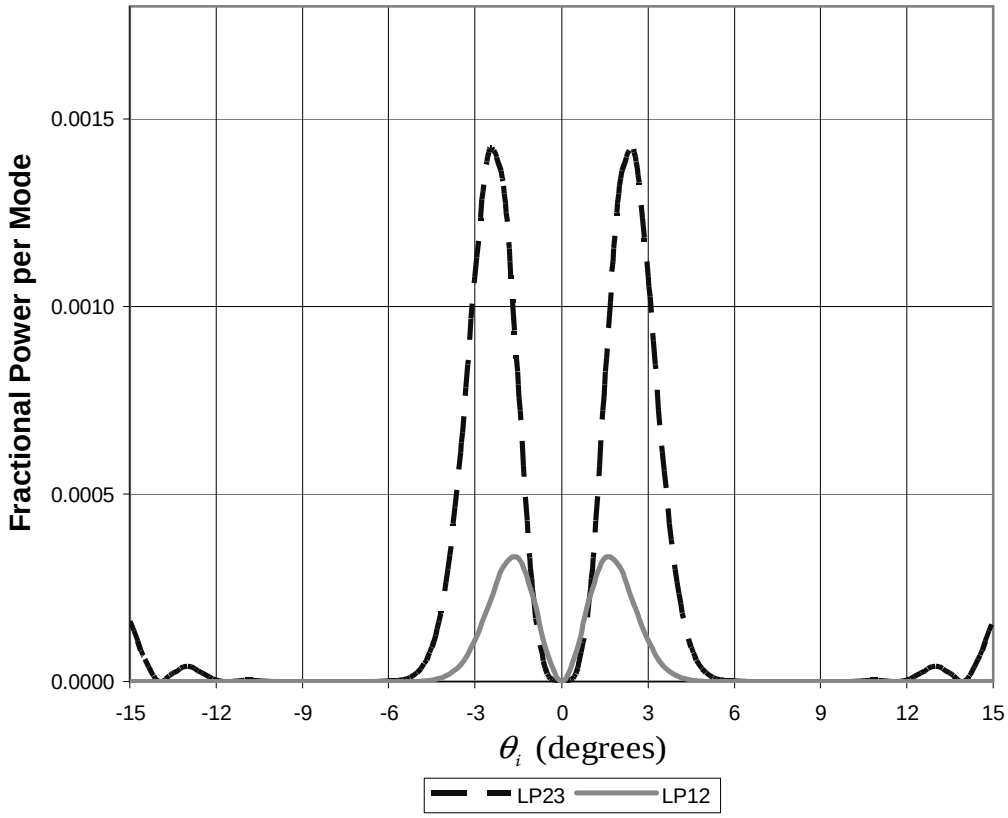

Figure 3.5 Fractional power for LP_{12} and LP_{23} as a function of the angle of incidence.

The fractional power in the l = 1, m = 3, 5, 7, 9, 13, 15, and 19 modes is plotted as a function of the angle of incidence in Fig. 3.6. Each curve has a trough at zero at normal incidence and peaks at two angles symmetrically positioned with respect to $\theta_i = 0$. The angle at which each curve peaks increases slightly as a function of m, which indicates that

the maximum power in each mode increases and occurs at different angles for the modes we considered. Notice that the maximum value for the l = 1, m = *3* peak is approximately five times higher than the peak for the other modes, which indicates that the LP_{13} mode transmits five times more power than the other l = 1 modes in the graph.

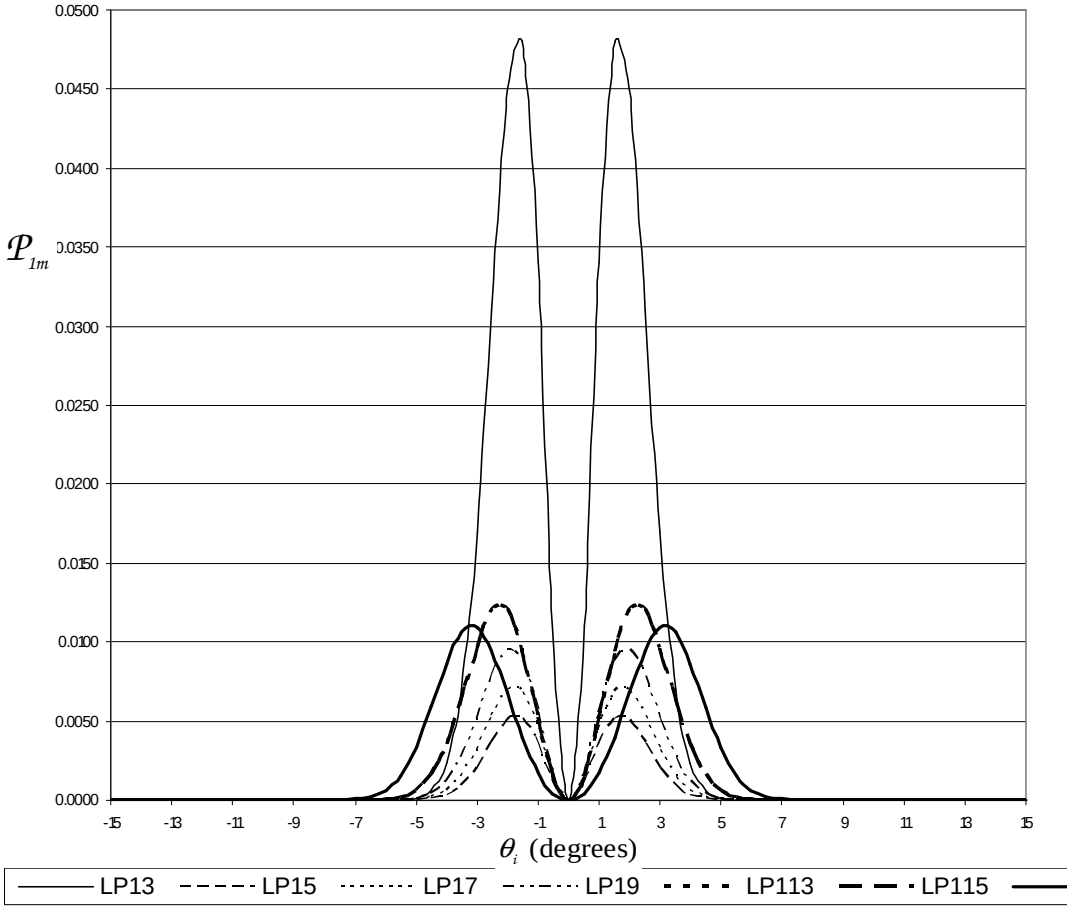

Figure 3.6 Fractional power for $l = 1$, m = 3, 5, 7, 9, 13, 15, 19 modes as a function of the angle of incidence.

In Fig. 3.7, the fractional power in the l = 2, m = 3, 4, 14, 15, 16, 17, 18, and 19 modes is plotted as a function of the angle of incidence. Similar to the l = 1 curves, each curve has a trough at zero at normal incidence and peaks at two angles symmetrically positioned with respect to $\theta_i = 0$. The increasing heights of the peaks tell us that the

maximum fractional power in each mode increases as a function of *m*. Also the peaks of the curves of higher *m* values, beginning with LP_{214}, are at least two times larger than the peaks of the curves of lower *m* values. This differs from the $l = 1$ curves in Fig. 3.6 where LP_{13} peaks approximately five times higher than the peaks for the curves of higher *m* values. This tells us that the maximum power for a given order $l > 1$ is not concentrated in the modes of lower *m* values as seen in $l = 0$ and $l = 1$. As previously stated, the power in LP_{21} and LP_{22} modes is very small. Also the power in the LP_{25} - LP_{213} modes is very small and thus these modes are not included in this graph.

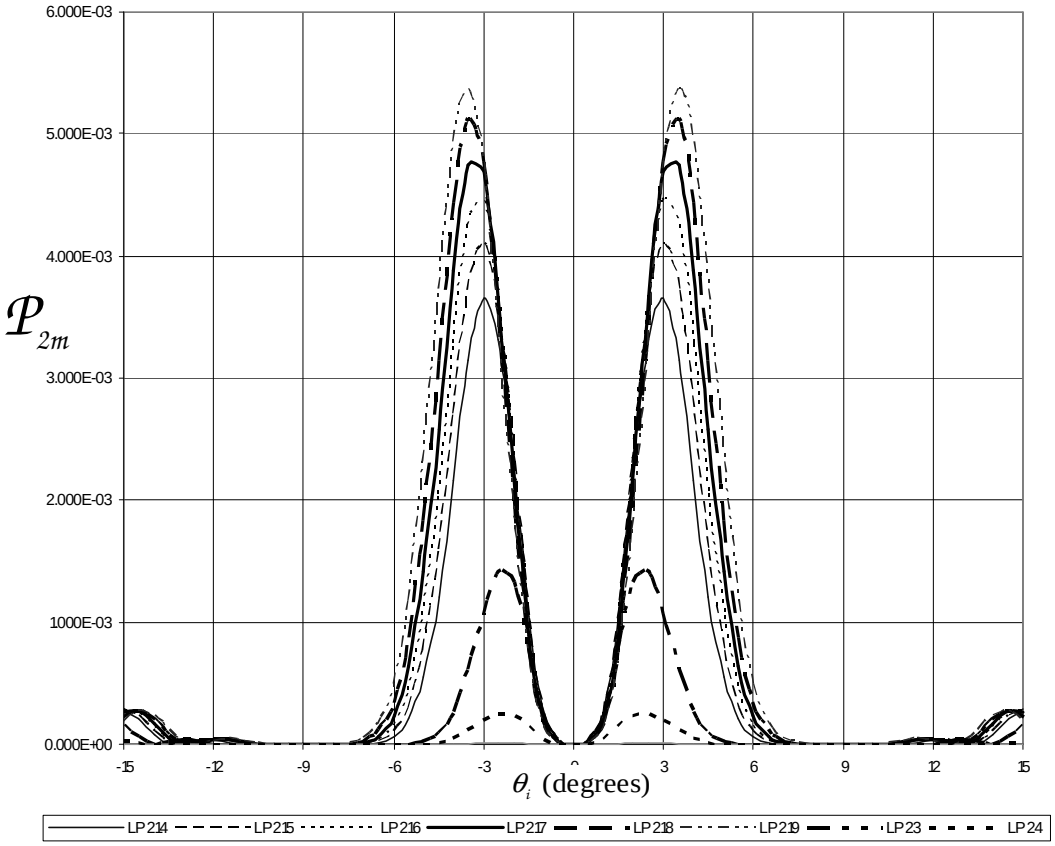

Figure 3.7 Fractional power for $l = 2$, $m = 3, 4, 14, 15, 16, 17, 18, 19$ modes versus the angle of incidence.

In Fig. 3.8, the fractional power in the l = 5, m = 13, 15, 17, and 19 modes is plotted as a function of the angle of incidence. Similar to the previous $l > 0$ modes, each curve has a trough at normal incidence. However, the curves differ in that each curve peaks and troughs at several additional angles that are symmetrically positioned with respect to $\theta_i = 0$. The increasing heights of the peaks for each curve tell us that the maximum fractional power in each mode increases as a function of m. The power in the $LP_{51} - LP_{512}$ modes is very small and thus these modes are not included in this graph.

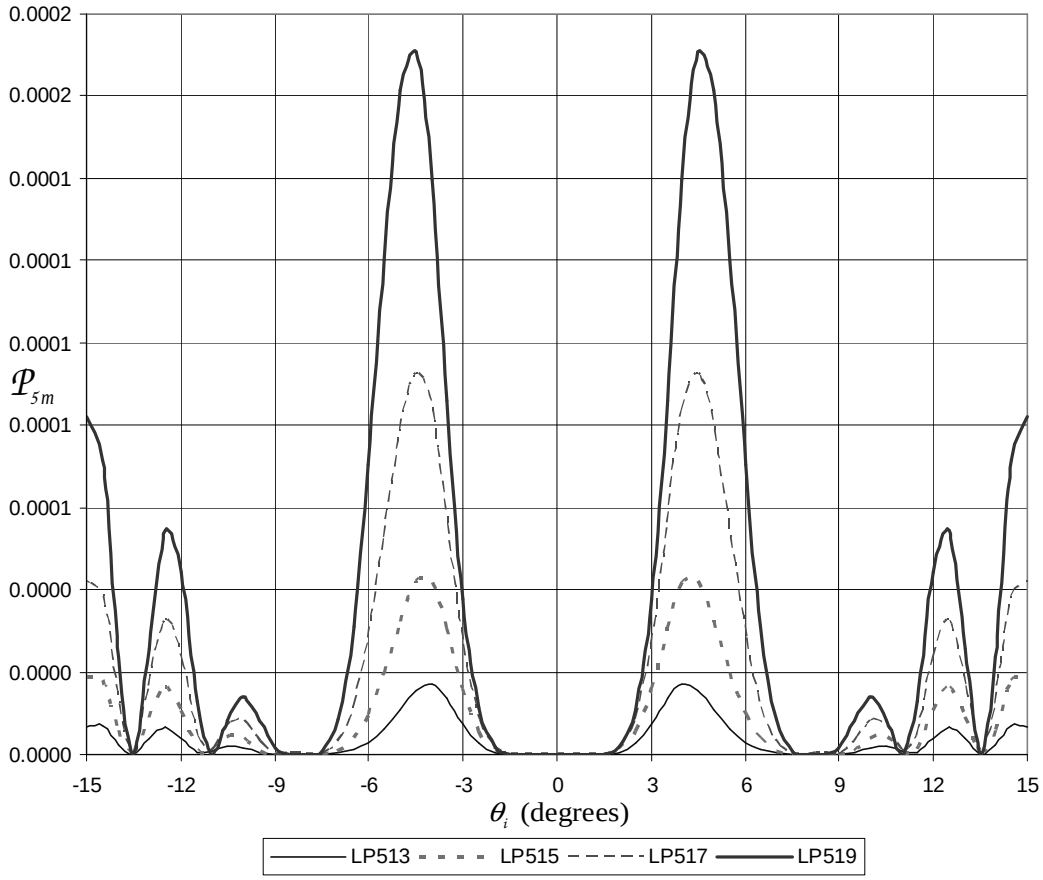

Figure 3.8 Fractional power for l = 5, m = 13, 15, 17, 19 modes as a function of the angle of incidence.

In Fig. 3.9, the fractional power in the l = 8, m = 11, 13, 15, 17, and 19 modes is plotted as a function of the angle of incidence. The power in the $LP_{81} - LP_{812}$ modes is very small and thus these modes are not included in this graph. Similar to the previous $l >$ 0 modes, each curve has a trough at zero at normal incidence. The curves are also similar to l = 5 with multiple troughs and peaks at angles symmetrically positioned with respect to $\theta_i = 0$. The curves differ, however, from l = 5 with sharper troughs in between each peak.

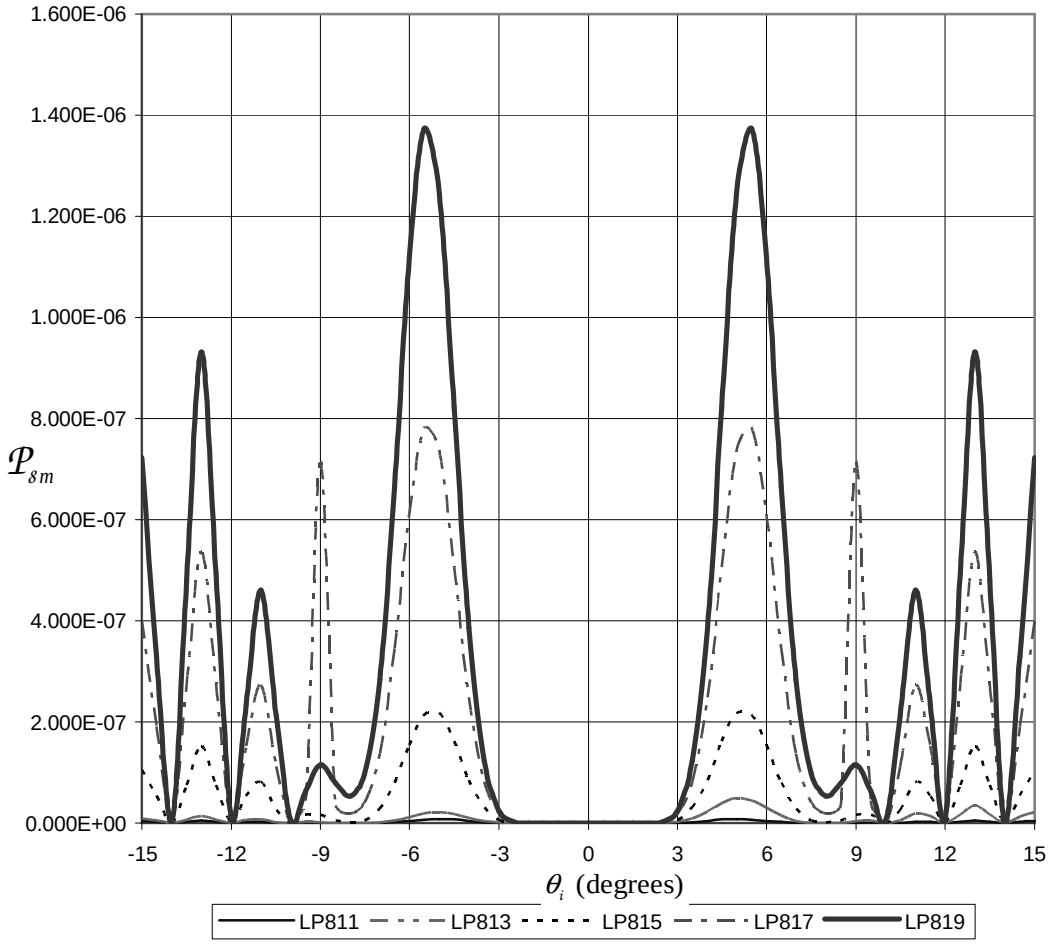

Figure 3.9 Fractional power for l = 8, m = 11, 13, 15, 17 and 19 modes as a function of the angle of incidence.

3.2.3 Fractional Power per Order and Total Fractional Power

The theoretical data in Table 3.3 illustrates the fractional power per order, $\mathcal{P}_l$, calculated with Eq. (3.48) for $\theta_i = 0^\circ, 5^\circ, 10^\circ$ and 15°. These tables agree with the graphs in Figs. 3.2-3.9 that illustrate the following relationships between lower and higher order modes and the angle of incidence. As θ_i increases, the power per mode in the lowest order (l = 0) modes decreases from an initial maximum at normal incidence while the power per mode in the higher order modes (l >1) is zero at normal incidence and, in general, nonzero for $\theta_i > 0^\circ$.

Table 3.3 Fractional power per order, $\mathcal{P}_l$, for the modes l = 0-8 for increasing values of θ_i.

l	θ=0°	θ=5°	θ=10°	θ=15°
0	9.798E-01	1.640E-02	0	3.000E-04
1	0	2.000E-03	0	3.000E-04
2	0	8.000E-03	7.473E-06	1.739E-03
3	0	4.300E-03	2.190E-05	5.940E-05
4	0	1.593E-03	3.411E-05	6.246E-06
5	0	4.540E-04	4.490E-05	2.430E-04
6	0	1.170E-04	3.770E-07	1.630E-05
7	0	2.530E-05	3.580E-06	4.840E-06
8	0	4.040E-06	9.190E-09	2.240E-06
SUM	9.798E-01	3.289E-02	1.123E-04	2.671E-03

The tabular data also provides information about the convergence of the series in Eq. (3.49). For $\theta_i = 0^\circ$, the data goes to zero rapidly indicating convergence of the series for the total power $\mathcal{P}$. For $\theta_i = 5^\circ$, the fractional power per mode is monotonically

decreasing, indicating convergence of the series for this angular position. However, for $\theta_i = 10^\circ$ and 15°, the data initially increases then oscillates, which does not provide sufficient information to determine convergence of the series. This non-convergence may be explained by error that results from limiting the factional power calculations to $l = 8$ because the peaks for the fractional power at $\theta_i = 10^\circ$ and 15° may occur at larger values of l. There may also be some error in the theoretical analysis from the use of the paraxial approximation in assuming a small angle for θ_i. The approximation is excellent for angles of fifteen degrees or less but gives an error of 3.53% for each use of the sine function for angle greater than fifteen degrees [9].

The graph in Fig. 3.10 plots the total fractional power in the fiber, calculated from Eq. (3.49), versus the angle of incidence. The graph tells us that total fractional power peaks at normal incidence and shows that the total fractional power in the fiber decreases as a function of the angle of incidence. This graph is compared with the experimental results for guided power of the large diameter fiber in Chapter IV.

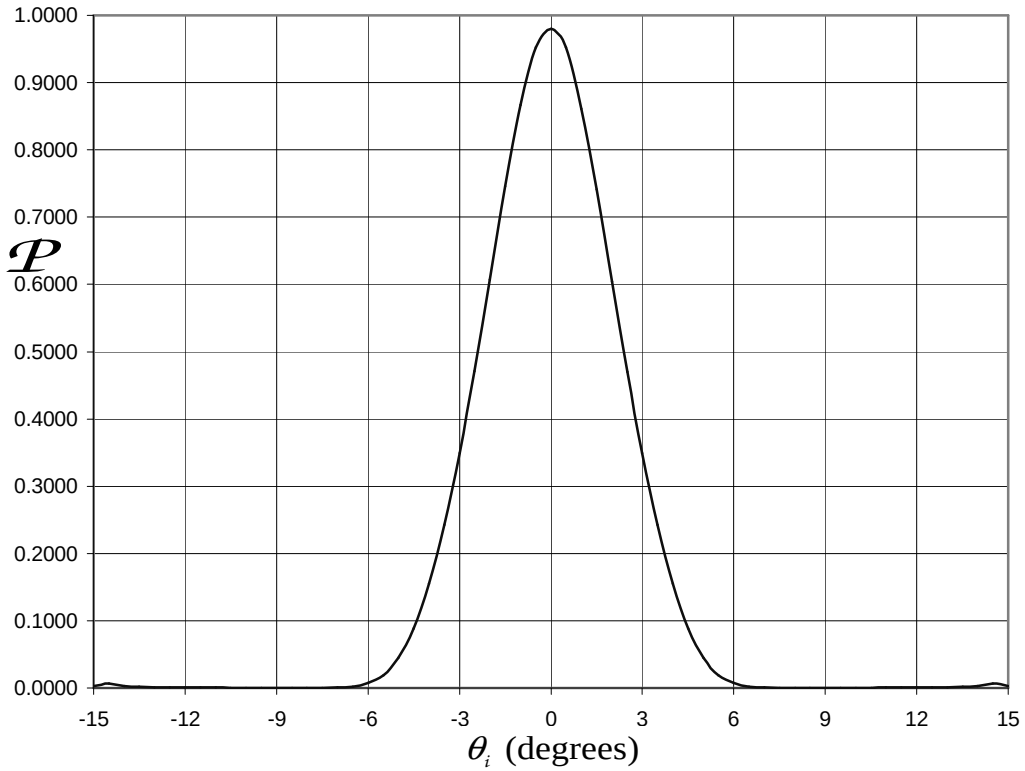

Figure 3.10 Total fractional power as a function of the angle of incidence.

3.3 Summary

In this chapter we derive a new expression, Eq. (3.47), for the fractional power per mode as a function of the angle of incidence for large radius fibers. Using the fractional power per mode, we see that each $l = 0$ modes exhibits a peak in fractional power at normal incidence. However, the higher order modes $l > 0$ peak at other angles of incidence and have a minimal fractional power when $\theta_i = 0$. The total fractional power in the fiber also peaks at normal incidence; it will be compared to the experimental results for varying the angle of incidence for a large diameter optical fiber in the next chapter.

CHAPTER IV

EXPERIMENT: VARYING THE ANGLE OF INCIDENCE ON A LARGE DIAMETER OPTICAL FIBER

In the previous chapter, an expression for the fractional power per mode as a function of the angle of incidence was derived. The expression was used to calculate total fractional and modal power for the modes of a large diameter optical fiber. In this chapter, we experimentally examine the effect of varying the angle of incidence on the total power guided in an optical fiber and compare the experimental and theoretical results.

4.1 Experimental Setup

The experimental setup is shown in Fig. 4.1. A plastic-clad silica fiber of 100μm core radius and 0.30 numerical aperture (NA) with n_1 = 1.474 having an approximate length of 0.50m was used in the present study [8]. The beam from a He-Ne laser (Melles-Griot, Model: 05-LLP-831) operating at 632.8nm was focused using an aspheric lens $\left(\text{Thorlabs, Inc., } f = 4.66\text{mm, NA} = 0.53\right)$ to couple light into one end of the fiber. As mentioned in Chapter II, the experimental fiber operating at this wavelength had a V = 298.6 and approximately 44,580 modes, which shows that the fiber is highly multimode.

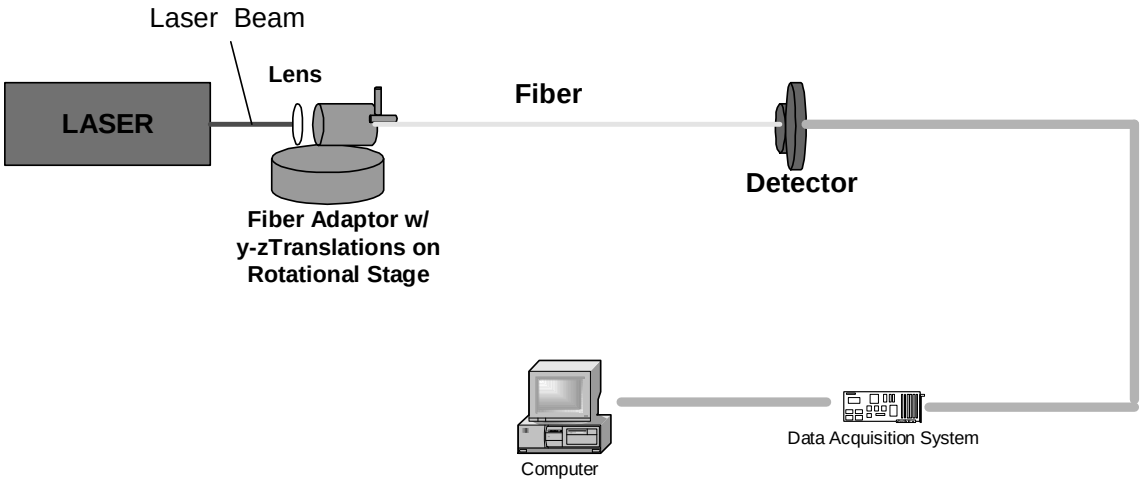

Figure 4.1 Experimental Setup

Prior to coupling the light into the fiber, both ends of the fiber were polished in order to achieve a smooth transverse surface. This end preparation is extremely critical in order to achieve good coupling efficiency. One end of the fiber was mounted on a fiber adapter for handling and positioning of the fiber. This adapter was then mounted over a *y-z* translation stage to align and position the fiber for maximum coupling of the light from the laser into the fiber. The translation stage was attached over a worm-driven rotational stage. This device allowed variation in the angular position of the fiber, which is the method used to varying the angle of incidence of the light into the fiber. The rotational stage was capable of continuously rotating a maximum of 360° in graduations of 2° increments with a vernier scale of 5 arc minute resolution. The fiber was mounted in such a way that the tip of the launching end of the fiber coincided with the axis of rotation as depicted in Fig. 4.2. This allowed a constant axis of rotation to be maintained. To

measure the guided optical power in the fiber, the other end of the fiber was connected to a detector (Thorlabs, Inc. Model No: PDA55).

The detector was connected to a data acquisition system to collect, display and store the value of the output power for each angle of incidence. The system consists of a National Instruments SCB-68 block to collect the data from the photo detector, a National Instruments PCI 6024E data acquisition board that connects to a personal computer and a LabView software module used to process and display the data graphically on the computer almost instantaneously [10]. This enabled the real-time monitoring of the experiment. LabView also stores the data for each experimental trial and allows exportation to an Excel file for data analysis.

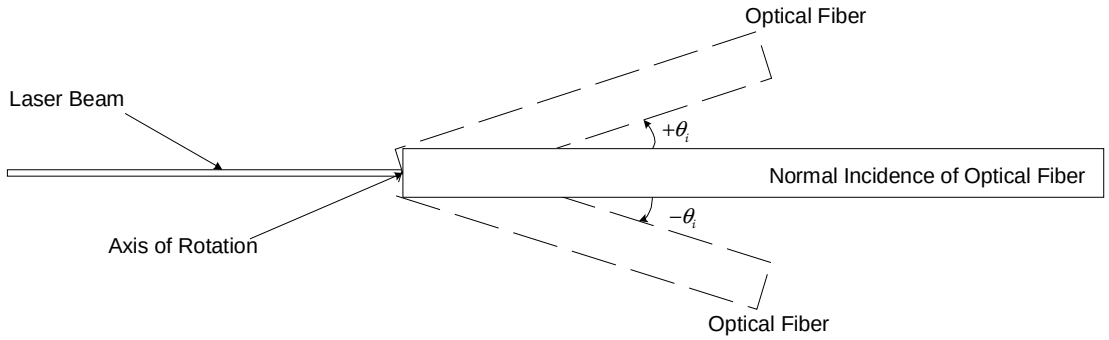

Figure. 4.2 Illustration of axis of rotation and angle of incidence of the experimental setup

4.2 Experimental Method

The optimum angular position of the fiber in the fiber holder was the position where maximum coupling was achieved, therefore, determining the position of normal incidence of the fiber. This position was determined before collecting data by varying the position of the fiber until the maximum brightness was observed on a detection screen.

The changes to increase to maximum brightness were made using the *y*-*z* translation stage on the fiber holder. Upon determining the maximum brightness on the detection screen, the fiber was connected to the detector for a more accurate determination of the maximum output power. Channel 1 in the data acquisition system read the optical power at the fiber output for changes made using the *y*-*z* -translation stages on the fiber adaptor holder, giving a maximum intensity of approximately 7 AU (Arbitrary Units).

The optimum orientation angle of the fiber, which corresponds to the optimum output power at the distal end of the fiber, was approximately 335° ± 2° as measured by the rotational scale of the worm-driven device. This optimum angle corresponds to the normal incidence ($\theta_i = 0°$, see Fig. 4.2) of the light into the fiber where the laser beam and the fiber axis are collinear. This optimum angle gives zero angular offset, which results in consistent observation of the highest fiber output. The maximum angular offset was limited by space constraints between the lens and fiber adaptor casings and experimentally observed to be 18° in both directions. Data was collected by varying the angle of incidence in 0.5° increments from a maximum angle 352° to a minimum angle 313°, which corresponds to a range of -18° to 18° with respect to the fiber axis.

4.3 Experimental Results and Analysis

The data for the guided optical power in the fiber was collected using a LabView module and converted into Microsoft Excel for analysis. The collected data was the measure of the guided power detected at the distal end of the fiber upon changing the angle of incidence of light entering the fiber from the He-Ne light source. The data was

normalized based on the maximum fiber output value obtained from each data set and is plotted in Figs. 4.3 and 4.4.

The following conclusions can be drawn from these results. First, the maximum optical power that could be launched into the fiber corresponds to normal incidence of the laser beam and the fiber axis. Second, almost identical optical power was launched in either direction of angular off-set, which is clearly depicted through the highly symmetric nature of the graphs with respect to normal incidence. Third, the optical power decreases as the

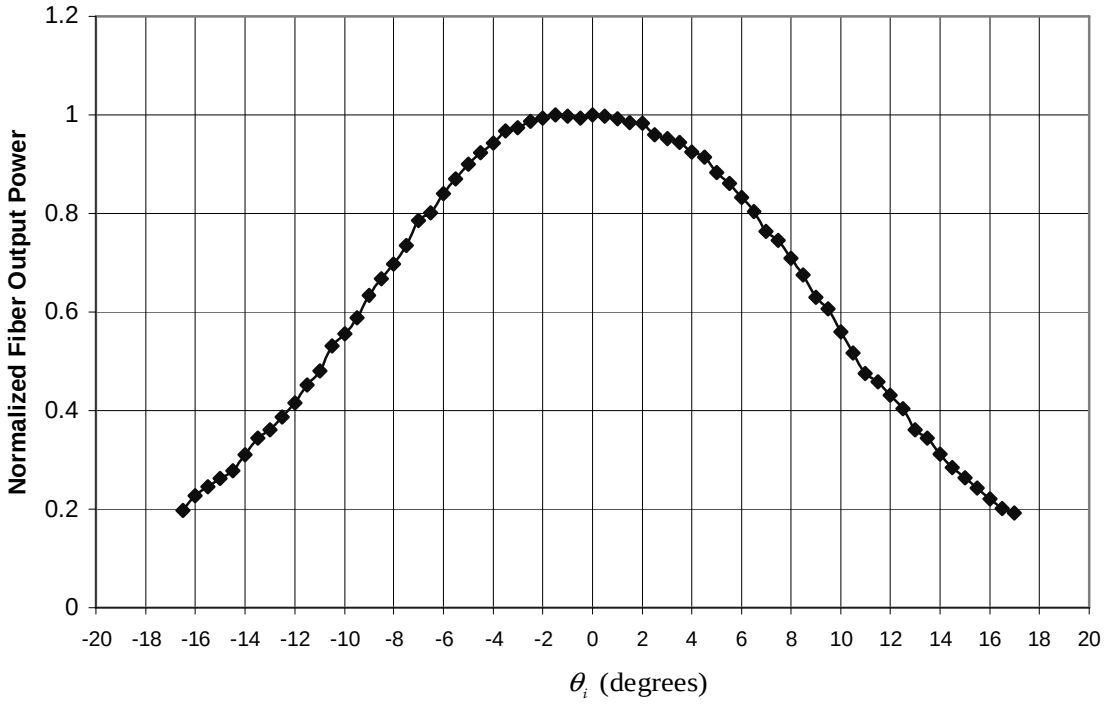

Figure 4.3 Normalized fiber output power as a function of the angle of incidence (data collected on April 13, 2004).

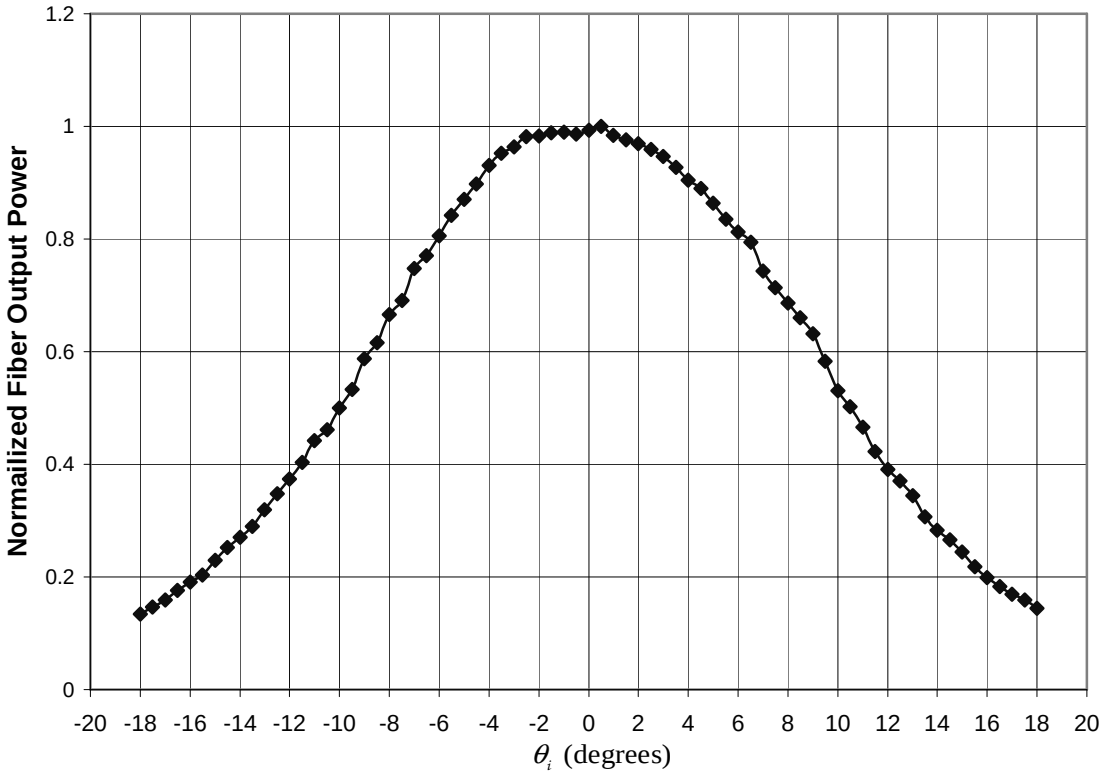

Figure 4.4 Normalized fiber output power as a function of the angle of incidence (data collected on April 16, 2004).

angle of incidence increases with respect to the fiber axis to a minimum of approximately 20% of the maximum amount of power coupled in the fiber. This shows that the experimental results qualitatively verify the theoretical results discussed in the previous chapter. However, these experimental results do not provide information about the amount of power in each mode of the fiber as seen in the theoretical results.

To compare and analyze the theoretical and experimental results for the total guided power in the optical fiber, the data obtained from the theoretical calculations in Chapter II (Fig. 3.2) is plotted with the average of the normalized experimental results (Figs. 4.3 and 4.4) in Fig. 4.5. Several conclusions can be drawn from this graph. First,

the peak at normal incidence tells us that maximum power occurs at normal incidence for both the theoretical and experimental data.

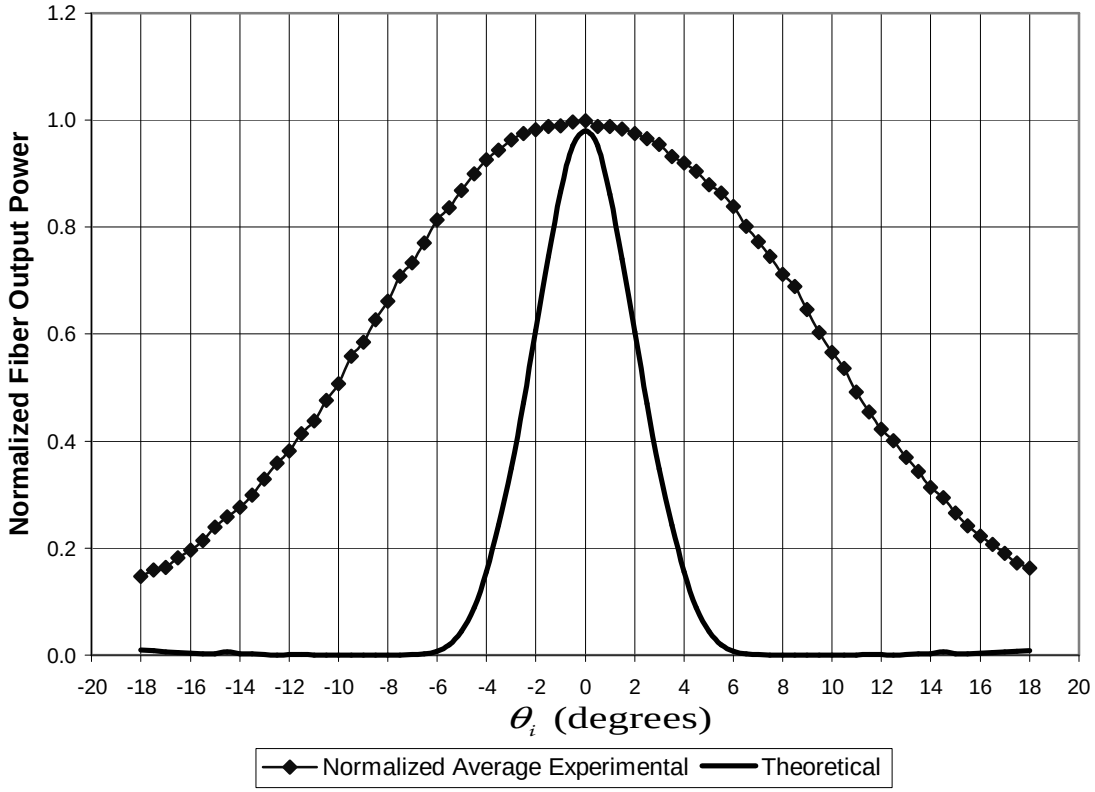

Figure 4.5 Normalized experimental output power and normalized theoretical output power as a function of the angle of incidence.

Fig 4.5 also tells us that the experimental data qualitatively verifies the theoretical data since both graphs show that the total power decreases as the angle of incidence increases. However, the experimental decrease is more gradual than the theoretical decrease. This may be due to the fact that the theoretical analysis was for 171 of approximately 44,580 modes. Although the amount of power in many of the individual higher order modes is small, the sum over them is probably non-negligible because they are so numerous. Thus, we conclude that determining the power for all possible modes

may give better agreement between the theoretical and experimental data. This conjecture is supported by the curves in Fig. 4.7, which plots the normalized total power for two theoretical cases, 32 (LP_{01}-LP_{84}) and 171 (LP_{01}-LP_{819}) modes, along with the average of the normalized experimental results. This plots shows that as more modes are considered in the analysis, the slope of the theoretical graphs becomes less steep. Therefore, increasing the number of modes in the theoretical analysis should provide results with better quantitative agreement with the experimental.

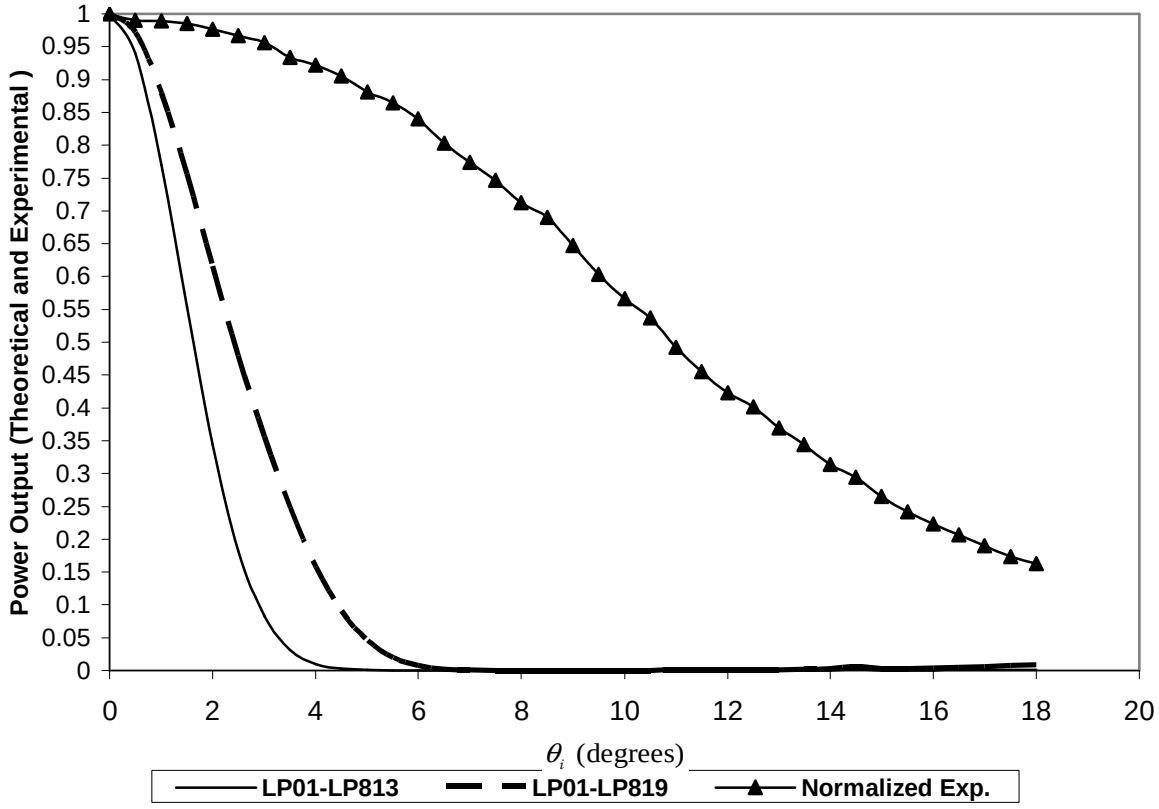

Figure 4.6 Normalized experimental output power and normalized theoretical output power as a function of the angle of incidence.

Also including the effects of the radiating modes may improve the quantitative agreement of the theoretical and experimental data.

4.4 Summary

The experimental examination of power guided in an optical fiber as a function of the angle of incidence showed that as the angle of incidence increased the power guided in the fiber decreased to approximately 20% of the maximum power in the fiber. Comparison of the experimental data with the theoretical data showed qualitative but not quantitative agreement. The presence of quantitative disagreement may be attributed to omitting power in modes beyond the initial 171 modes and not accounting for radiation modes.

CHAPTER V

DISCUSSIONS AND CONCLUSIONS

The basic theory for the modes of a weakly, guiding, step index fiber was presented in Chapter II, along with the analytical approximation technique of Gloge. In Chapter III a new expression [Eq. (3.47)] was derived for the fractional power per mode of a large diameter, weakly-guiding, step-index fiber.

This expression was used to obtain numerical values for the fractional power per mode, $P_l / P_i = \mathcal{P}_{lm}$, power per order, $\mathcal{P}_l$, and total power, $\mathcal{P}$. Graphical and tabular analysis of the fractional power per mode and per order illustrate that l = 0 modes transmit the maximum amount of power for normal incidence ($\theta_i = 0^\circ$) with LP_{01} transmitting 50% of the power when $\theta_i = 0^\circ$. It is shown that the l = 0 modes transmit all of the power at this angle, it follows that modes for $l > 0$ contained no power at $\theta_i = 0^\circ$. However, these higher l value modes transmit more of the power than the l = 0 modes for $\theta_i \neq 0^\circ$ The transition in the amount of fractional power per mode from modes of low l values to modes of higher l values for larger angles of incidence leads us to believe that for the larger angles of incidence, more than the 171 modes, considered here need to be included.

In Chapter IV, the experimental investigation of power guided in an optical fiber as a function of the angle of incidence was presented. The experimental results showed that as the angle of incidence increased the power guided in the fiber decreased to approximately 20% of the maximum power. By comparing the theoretical results to the experimental results, we conclude that the theoretical method is accurate for very small angles. We also notice that the theoretical and experiment results agree qualitatively but not quantitatively at larger angles. The disagreement between the theoretical and experimental results is most likely due to omitting the higher order modes.

Future work from this thesis could have several different theoretical, computational and experimental approaches. Theoretically, one could obtain expressions for higher order zeros of the Bessel functions and use then in Eq. (3.47) to calculate the power in the higher order modes. This theoretical work could be combined with computational physics techniques to calculate all the power in the approximate 44,580 modes, which would eliminate the matrix limitations associated with this method. Experimentally, variance of the angle of incidence to excite specific modes need for specialized sensing locations and requirements for straight, bent and tapered optical fiber sensors could result in new sensing techniques.

APPENDIX A

EXAMPLE MATHCAD WORKSHEET

$n_1 := 1.474$ $n_2 := 1.443$ $a := 100$ $\lambda_0 := .6328$ $k_0 := \frac{(2 \cdot \pi)}{\lambda_0}$ $k_0 =$ $A := 1$

$\theta := 0.5 , 1.0 .. 18$

$K(\theta) := a \cdot k_0 \cdot \theta \cdot \left(\frac{\pi}{180}\right)$

$l := 4$ $m := 3$

$V := k_0 \cdot a \left[(n_1)^2 - (n_2)^2 \right]^{\left(\frac{1}{2}\right)}$ $V =$

$M_l :=$

1 if (0 < V < 2.40482)
2 if (2.40483 < V < 5.52007)
3 if (5.52007 < V < 8.65372)
4 if (8.65372 < V < 11.79153)
5 if (11.79153 < V < 14.93091)
6 if (14.93091 < V < 18.07106)
7 if (18.07106 < V < 21.21163)
8 if (21.21163 < V < 24.35247)
9 if (24.35247 < V < 27.49347)
10 if (27.49347 < V < 30.63460)
11 if (30.63460 < V < 33.77582)

$M_l =$

$uc :=$

0	3.83171	7.01559	10.17347	13.32369
0	2.40482	5.52007	8.65372	11.79153
0	3.83171	7.01559	10.17347	13.32369
0	5.13562	8.41724	11.61984	14.79595
0	6.38016	9.76102	13.01520	16.22347
0	7.58834	11.06471	14.37254	17.61597
0	8.77148	12.33860	15.70017	18.98013
0	9.93611	13.58929	17.00382	20.32079
0	11.08637	14.82127	18.28758	21.64154

$uc_{(l,m)} =$

$s_{(l,m)} := \sqrt{\left[uc_{(l,m)}\right]^2 - l^2 - 1}$

$w := \operatorname{asin}\left[\frac{s_{(l,m)}}{uc_{(l,m)}}\right] - \operatorname{asin}\left[\frac{s_{(l,m)}}{V}\right]$ $w =$

$r_1 := \exp\left[\frac{w}{s_{(l,m)}}\right]$ $r_1 =$

$g := uc_{(l,m)} \cdot r_1$

$U :=$ 1 if $m = 0$; g otherwise $U =$

This formula is incorrect for l = 0 and m = 1. That case will be done in a separate mathcad document.

$W := \sqrt{V^2 - U^2}$ $\quad U =$ $\quad W =$

$N := 80$ $\quad i := 0 .. N$ $\quad j := 0 .. N$ $\quad \delta x := \frac{3 \cdot a}{N}$

$x_i := -1.5 \cdot a + i \cdot \delta x$ $\quad y_j := -1.5 \cdot a + j \cdot \delta x$

$r(\xi, \eta) := \sqrt{\xi^2 + \eta^2}$

$$\phi(\xi, \eta) := \begin{cases} 0 & \text{if } r(\xi, \eta) = 0 \\ \operatorname{atan2}(\xi, \eta) & \text{otherwise} \end{cases}$$

$$f(\xi, \eta) := \frac{Jn\left(l, \frac{U \cdot r(\xi, \eta)}{a}\right) \cdot A \cdot \cos(l \cdot \phi(\xi, \eta))}{Jn(l, U)} \qquad g(\xi, \eta) := \frac{Kn\left(l, \frac{W \cdot r(\xi, \eta)}{a}\right) \cdot A \cdot \cos(l \cdot \phi(\xi, \eta))}{Kn(l, W)}$$

$$\psi(\xi, \eta) := \begin{cases} f(\xi, \eta) & \text{if } r(\xi, \eta) < a \\ g(\xi, \eta) & \text{otherwise} \end{cases} \qquad D(\theta) := \frac{60}{K(\theta)}$$

$$C(\theta) := \frac{1}{\left(\left| Jn(l, U) \right|\right)^2} \cdot \begin{cases} \left[\left[\int_0^1 e^{\left(\frac{-R^2 \cdot a^2}{5^2}\right)} \cdot Jn(l, U \cdot R) \cdot Jn(l, K(\theta) \cdot R) \cdot R \, dR \right] \right]^2 & \text{if } D(\theta) > 1 \\ \left[\left[\int_0^{0.989} e^{\left(\frac{-R^2 \cdot a^2}{5^2}\right)} \cdot Jn(l, U \cdot R) \cdot Jn(l, K(\theta) \cdot R) \cdot R \, dR + \sqrt{\frac{2}{\pi \cdot K(\theta)}} \cdot \int_{0.989}^1 e^{\left(\frac{-R^2 \cdot a^2}{5^2}\right)} \cdot Jn(l, U \cdot R) \cdot \cos\left[K(\theta) \cdot R - \left(l + \frac{1}{2}\right) \cdot \frac{\pi}{2} \right] \cdot \sqrt{R} \, dR \right] \right]^2 & \text{otherwise} \end{cases}$$

$$P(\theta) := \left[4 \cdot n_1 \cdot a^2 \cdot \left(\frac{U}{V}\right)^2 \cdot \frac{C(\theta)}{5^2} \right]$$

K(θ)	C(θ)	P(θ)
8.665	1.44E-13	7.83E-13
17.33	2.80E-11	1.52E-10
25.995	4.54E-10	2.47E-09
34.659	2.39E-09	1.30E-08
43.324	6.25E-09	3.41E-08
51.989	9.83E-09	5.36E-08
60.654	1.03E-08	5.60E-08
69.319	7.58E-09	4.13E-08
77.984	4.11E-09	2.24E-08
86.648	1.69E-09	9.21E-09
95.313	5.49E-10	2.99E-09
103.978	1.47E-10	8.03E-10
112.643	2.82E-11	1.54E-10
121.308	1.10E-13	5.99E-13
129.973	1.48E-11	8.08E-11
138.638	2.86E-11	1.56E-10
147.302	6.55E-13	3.57E-12
155.967	1.02E-10	5.53E-10
164.632	4.28E-10	2.33E-09
173.297	3.93E-10	2.14E-09
181.962	1.24E-12	6.75E-12
190.627	7.85E-10	4.28E-09
199.291	2.33E-09	1.27E-08
207.956	1.79E-09	9.78E-09
216.621	9.00E-11	4.91E-10
225.286	1.06E-09	5.78E-09
233.951	3.59E-09	1.96E-08
242.616	3.45E-09	1.88E-08
251.28	1.05E-09	5.71E-09

259.945	1.15E-11	6.26E-11
268.61	1.02E-09	5.54E-09
277.275	1.92E-09	1.05E-08
285.94	1.56E-09	8.47E-09
294.605	6.34E-10	3.45E-09
303.27	7.96E-11	4.34E-10
311.934	1.43E-11	7.78E-11

APPENDIX B:

DERIVATION OF EQ. (3.14)

The following well-known integrals are used to evaluate Eq. (3.12). In $B_l^{(1)}$,

$$B_l^{(1)}(R) = J_0(\kappa R)\int_0^{2\pi}\cos(l\phi)\,d\phi + 2\sum_{p=1}^{\infty} i^p J_p(\kappa R)\int_0^{2\pi}\cos(p\phi)\cos(l\phi)\,d\phi \qquad (B1)$$

the first integral is evaluated with

$$\int_0^{2\pi}\cos(l\phi)\,d\phi = \begin{cases} 0, & l \neq 0 \\ 2\pi, & l = 0 \end{cases} \qquad (B2)$$

which yields

$$J_0(\kappa R)\int_0^{2\pi}\cos(l\phi)\,d\phi = 2\pi J_0(\kappa R)\,\delta_{l,0}. \qquad (B3)$$

The next integral in (B1) is evaluated with

$$\int_0^{2\pi}\cos(p\phi)\cos(l\phi)\,d\phi = \begin{cases} 0, & p \neq l,\ l = 0 \\ \pi, & p = l,\ l \neq 0 \end{cases} = \pi\delta_{p,l},\ l = 1,2,\ldots \qquad (B4)$$

which yields

$$2\sum_{p=1}^{\infty} i^p J_p(\kappa R)\int_0^{2\pi}\cos(p\phi)\,d\phi\cos(l\phi)\,d\phi = 2i^p J_p(\kappa R)\pi\delta_{p,l}, \quad \text{for } p = l \neq 0. \qquad (B5)$$

Thus, the result is

$$B_l^{(1)}(R) = \begin{cases} 2\pi J_0(\kappa R), & l = 0 \\ 2\pi i^l J_l(\kappa R), & l \neq 0 \end{cases}. \qquad (B6)$$

Now considering $B_l^{(2)}(R)$ where $l \neq 0$ but $l = 1,2,\ldots$

$$B_l^{(2)}(R) = J_0(\kappa R)\int_0^{2\pi}\sin(l\phi)\,d\phi + 2\sum_{p=1}^{\infty} i^p J_p(\kappa R)\int_0^{2\pi}\sin(p\phi)\cos(l\phi) \qquad (B7)$$

where

$$\int_0^{2\pi}\sin(l\phi)\,d\phi = 0$$
$$\int_0^{2\pi}\sin(p\phi)\cos(l\phi)d\phi = 0. \qquad (B8)$$

$$B_l^{(1)}(R) = \begin{cases} 2\pi J_0(\kappa R), & l = 0 \\ 2\pi i^l J_l(\kappa R), & l \neq 0 \end{cases} \qquad (B9)$$

and

$$B_l^{(2)}(R) = 0 \qquad (B10)$$

where for Eq. (3.15) when $l = 0$, $i^0 = 1$ shows that the second term results in the first term when $l = 0$. Therefore,

$$B_l^{(1)}(R) = 2\pi i^l J_l(\kappa R), \quad l = 0,1,\ldots \qquad (B11)$$

APPENDIX C:

DERIVATION OF EQ. (3.23)

To derive an asymptotic expression for the cladding integral in (4.13b) for the case of $\bar{R}_l < 1$, we begin with the following expression that results from using the asymptotic forms of $J_l(x)$ and $K_l(x)$

$$I_l^{(2)} = \sqrt{\frac{2}{\pi\kappa}} \int_1^\infty \exp\left[-\gamma^2 R^2 - WR - W\right] \cos\left[\kappa R - \left(l + \frac{1}{2}\right)\frac{\pi}{2}\right] dR \qquad (C1)$$

where

$$\cos\left[\kappa R - \frac{\pi}{2}\left(l + \frac{1}{2}\right)\right] = \mathrm{Re}\left\{\exp - i\left[\kappa R - \left(l + \frac{1}{2}\right)\frac{\pi}{2}\right]\right\} \qquad (C2)$$

gives

$$I_l^{(2)} = \sqrt{\frac{2}{\pi\kappa}}\,\mathrm{Re}\left\{\exp\left[i\left(l + \frac{1}{2}\right)\frac{\pi}{2}\right]\int_1^\infty \exp\left[-\gamma^2 R^2 - (W + i\kappa)R + W\right] dR\right\}. \qquad (C3)$$

Completing the square for the $\exp\left[-\gamma^2 R^2 - (W + i\kappa)R + W\right]$ term and factoring out the real terms that do not depend on *R* gives the following

$$I_l^{(2)} = \sqrt{\frac{2}{\pi\kappa}} \exp\left[W + \frac{W^2}{4} - \frac{\kappa^2}{4}\right] \mathrm{Re}\left\{\begin{array}{l} \exp\left\{i\left[\left(l + \frac{1}{2}\right)\frac{\pi}{2} + \frac{\kappa W}{2}\right]\right\} \\ \qquad \times \int_1^\infty \exp\left[-\gamma^2\left(R + \frac{(W + i\kappa)^2}{2\gamma^2}\right)^2\right] dR \end{array}\right\} \qquad (C4)$$

where the remaining integral can be expressed as a complementary error function, *erfc*(*z*). defined as follows

$$erfc(z) = \frac{2}{\sqrt{\pi}} \int_z^\infty e^{-t^2} dt\,. \qquad (C5)$$

Letting

$$t = \gamma\left(R + \frac{(W + i\kappa)^2}{2\gamma^2}\right) \qquad (C6)$$

gives

$$I_l^{(2)} \approx \frac{1}{2\gamma}\sqrt{\frac{2}{\pi\kappa}}\exp\left[W+\frac{W^2}{4}-\frac{\kappa^2}{4}\right]\mathrm{Re}\left\{\begin{array}{l}\exp\left\{i\left[\left(l+\frac{1}{2}\right)\frac{\pi}{2}+\frac{\kappa W}{2}\right]\right\}\\ \qquad\times erfc\left\{\gamma\left[1+\frac{(W+i\kappa)^2}{2\gamma^2}\right]\right\}\end{array}\right\} \quad (C7)$$

Since $W \approx 300$, we use the asymptotic form of the complementary error function given in

$$erfc(z) \sim \frac{1}{\sqrt{\pi}z\exp\left(z^2\right)}, \quad \text{as } z \to \infty. \quad (C8)$$

Expressing the complementary error function in these terms gives

$$I_l^{(2)} \approx \frac{1}{2\gamma}\sqrt{\frac{2}{\pi\kappa}}\exp\left[W+\frac{W^2}{4}-\frac{\kappa^2}{4}\right]\mathrm{Re}\left\{\begin{array}{l}\exp\left\{i\left[\left(l+\frac{1}{2}\right)\frac{\pi}{2}+\frac{\kappa W}{2}\right]\right\}\\ \qquad\frac{1}{\gamma\left[1+\frac{(W+i\kappa)^2}{2\gamma^2}\right]\exp\left[\gamma\left(1+\frac{(W+i\kappa)^2}{2\gamma^2}\right)\right]^2}\end{array}\right\} \quad (C9)$$

Expanding the quadratic terms, consolidating common powers and returning to the cosine representation gives the asymptotic approximation for $I_l^{(2)}$

$$I_l^{(2)} = C_1\left[\frac{\exp\left[-\left(\frac{W^4}{4\gamma^2}-qW^2-W\right)\right]}{\Omega(W)}\cos\left[\Lambda(W)+\left(l+\frac{1}{2}\right)\frac{\pi}{2}\right]\right], \quad (C10)$$

$$q_1 = \frac{3}{2}+\frac{\kappa^2}{\gamma^2}-\frac{3}{4}, \quad (C11)$$

$$C_1 = \frac{1}{2\pi\gamma^2}\sqrt{\frac{2}{\kappa}}\exp\left[\sigma_1\kappa^2-\frac{\kappa^4}{4\gamma^2}+\gamma^2\right], \quad (C12)$$

$$\sigma_1 = -\frac{1}{4}+\gamma^2, \quad (C13)$$

$$\Omega_1(W) = 1+\frac{W^2}{2\gamma^2}-\frac{\kappa^2}{2\gamma^2}, \quad (C14)$$

$$\Lambda_1(W) = \frac{\kappa W^3}{\gamma^2} - \frac{\kappa^3 W}{4\gamma^4} - \frac{3}{2}\kappa W. \qquad (C15)$$

APPENDIX D:

DERIVATION OF ASYMPTOTIC APPROXIMATE UPPER BOUND FOR EQ. (3.35)

To determine the asymptotic approximation upper limit, the concept that the absolute value of $I_l^{(3)}$ must be less than or equal to the integral of the absolute value, is expressed in

$$\left|I_l^{(3)}\right| \le \int_1^{\bar{R}_l} \left|g\left(R\right)\right| \left|J_l\left(\kappa R\right)\right| \sqrt{R} dR \qquad (D1)$$

where analysis of each function in Eq. (4.23) gives

$$\left|g\left(R\right)\right| > 0 \qquad (D2)$$

$$\left|J_l\left(\kappa R\right)\right| \le 1. \qquad (D3)$$

Therefore, the Bessel function is not included in the integral and evaluation of the following integral will result in an expression for $I_l^{(3)}$

$$\left|I_l^{(3)}\right| \le \sqrt{\bar{R}_l} \int_1^{\bar{R}_l} \exp\left[-\gamma^2 R^2 - WR + W\right] dR \qquad (D4)$$

After completing the square,

$$\left|I_l^{(3)}\right| \le \sqrt{\bar{R}_l} \exp\left[W\left(1 + \frac{W}{4\gamma^2}\right)\right] \int_1^{\bar{R}_l} \exp\left[-\gamma^2\left(R^2 + \frac{W}{2\gamma^2}\right)^2\right] dR \qquad (D5)$$

In order to evaluate the integral in (*D*4), we begin by recognizing that the integral may be written as an error function defined as

$$erf\left(z\right) = \frac{2}{\sqrt{\pi}} \int_0^z e^{-t^2} dt \qquad (D6)$$

To put Eq. (*D*4) into error function form, we let

$$t = \gamma\left(R + \frac{W}{2\gamma^2}\right), \qquad (D7)$$

which gives

$$\int_1^{\bar{R}_l} \exp\left[-\gamma^2\left(R^2+\frac{W}{2\gamma^2}\right)^2\right] = \frac{1}{\gamma}\int_{\gamma\left(1+\frac{W}{2\gamma^2}\right)}^{\gamma\left(\bar{R}_l+\frac{W}{2\gamma^2}\right)} \exp\left(-t^2\right)dt$$

$$= \frac{1}{\gamma}\left[\int_0^{\gamma\left(\bar{R}_l+\frac{W}{2\gamma^2}\right)} \exp\left(-t^2\right)dt - \int_0^{\gamma\left(1+\frac{W}{2\gamma^2}\right)} \exp\left(-t^2\right)dt\right] \quad (D8)$$

$$= \frac{\sqrt{\pi}}{2\gamma}\left\{erf\left[\gamma\left(\bar{R}_l+\frac{W}{2\gamma^2}\right)\right] - erf\left[\gamma\left(1+\frac{W}{2\gamma^2}\right)\right]\right\}$$

Since $W \approx 300$, an asymptotic form of the error function is needed to further evaluate the expression. We use the complementary error function, $erfc(z)$ asymptotic form, defined in

$$erfc(z) \sim \frac{1}{z\exp\left(z^2\right)}. \quad (D9)$$

We define the result from the integral in $\left|I_l^{(3)}\right|$ as $\left|I_l^{(3a)}\right|$ in

$$\left|I_l^{(3a)}\right| = \frac{\sqrt{\pi}}{2\gamma}\left\{erf\left[\gamma\left(\bar{R}_l+\frac{W}{2\gamma^2}\right)\right] - erf\left[\gamma\left(1+\frac{W}{2\gamma^2}\right)\right]\right\} = \left\{E_1 - E_2\right\} \quad (D10)$$

where

$$E_1 = \frac{1}{\gamma\left(1+\frac{W}{2\gamma^2}\right)\exp\left[\gamma\left(1+\frac{W}{2\gamma^2}\right)\right]^2} \quad (D11)$$

$$E_2 = \frac{1}{\gamma\left(\bar{R}_l+\frac{W}{2\gamma^2}\right)\exp\left[\gamma\left(\bar{R}_l+\frac{W}{2\gamma^2}\right)\right]^2} \quad (D12)$$

result from the asymptotic form of the *erfc* function.

Therefore, it follows that

$$\left|I_l^{(3)}\right| \le \frac{\sqrt{\bar{R}_l}}{\gamma}\left|\exp\left[W\left(1+\frac{W}{4\gamma^2}\right)\right]\left(E_1 - E_2\right)\right| \qquad (D13)$$

Algebraic manipulation of Eq. (*D*13) results in cancellation of the $\exp\left[W/4\gamma^2\right]$ term, such that

$$\left|I_l^{(3)}\right| \le \frac{\sqrt{\bar{R}_l}}{\gamma}\left|\exp\left(W\right)\left(E_1' - E_2'\right)\right| \qquad (D14)$$

where

$$E_1' = \frac{1}{\left(1+\frac{W}{2\gamma^2}\right)\exp\left[\gamma^2\left(1+\frac{W}{\gamma^2}\right)\right]} \qquad (D15)$$

$$E_2' = \frac{1}{\left(\bar{R}_l+\frac{W}{2\gamma^2}\right)\exp\left[\gamma^2\left(\bar{R}_l^2+\frac{W\bar{R}_l}{\gamma^2}\right)\right]} \qquad (D16)$$

APPENDIX E:

DERIVATION OF EQ. (3.36)

To solve for an analytic approximation expression for

$$I_l^{(4)} = \sqrt{\frac{2}{\pi\kappa}} \int_{\bar{R}_l}^{\infty} g(R) \cos\left[\kappa R - \frac{\pi}{2}\left(l + \frac{1}{2}\right)\right] dR . \qquad (E1)$$

where

$$\cos\left[\kappa R - \frac{\pi}{2}\left(l + \frac{1}{2}\right)\right] = \mathrm{Re}\left\{\exp - i\left[\kappa R - \frac{\pi}{2}\left(l + \frac{1}{2}\right)\right]\right\}. \qquad (E2)$$

Inputting $g(R)$, Eq. (3.22a), and factoring terms that do not depend on R out of the integral gives

$$I_l^{(4)} = \sqrt{\frac{2}{\pi\kappa}}\, \mathrm{Re}\left\{\exp i\left(l + \frac{1}{2}\right)\frac{\pi}{2} \exp\left(W + \frac{(W + i\kappa)^2}{4}\right) \int_{\bar{R}_l}^{\infty} \exp\left\{-\gamma^2\left[\left(R + \frac{(W + i\kappa)^2}{2\gamma^2}\right)^2\right]\right\} dR\right\} \qquad (E3)$$

The integral is evaluated in terms of an error function as shown in Appendix E to give the following result

$$I_l^{(4)} = \frac{1}{2\gamma}\sqrt{\frac{2}{\kappa}}\, \mathrm{Re}\left\{\exp i\left(l + \frac{1}{2}\right)\frac{\pi}{2} \exp\left(W + \frac{(W + i\kappa)^2}{4}\right) erfc\left\{\gamma\left[\bar{R}_l + \frac{(W + i\kappa)^2}{2\gamma^2}\right]\right\}\right\}. \qquad (E4)$$

Since $W \approx 300$ is included in the argument of the complementary error function term, we use the functions asymptotic form given in Eq. (3.2) as $z \gg 1$. The use of the asymptotic form gives the following

$$I_l^{(4)} = \frac{1}{2\gamma}\sqrt{\frac{2}{\kappa}} \exp\left(W + \frac{W^2}{4} - \frac{\kappa^2}{4}\right) \mathrm{Re}\left\{\exp\left[i\left(l + \frac{1}{2}\right)\frac{\pi}{2} + \frac{\kappa W}{2}\right] \frac{1}{\sqrt{\pi}\left\{\gamma\left[\bar{R}_l + \frac{(W + i\kappa)^2}{2\gamma^2}\right]\right\} \exp\left[\gamma\left(\bar{R}_l + \frac{(W + i\kappa)^2}{2\gamma^2}\right)\right]^2}\right\} \qquad (E5)$$

After algebraic manipulation of Eq. (3.33) shown (in Appendix E), the follows expression results

$$I_l^4 = C_2 \frac{\exp\left[-\left(\frac{W^4}{4\gamma^2} - q_2 W^2 - W - \eta \bar{R}_l\right)\right]}{\Omega_2(W)} \cos\left[\Lambda_2(W) + \left(l + \frac{1}{2}\right)\frac{\pi}{2}\right] \tag{E6}$$

where

$$q_2 = \frac{1}{4} + \frac{3\kappa^2}{2\gamma^2} - \bar{R}_l \tag{E7}$$

$$\eta = \gamma^2 \bar{R}_l - \kappa^2 \tag{E8}$$

$$C_2 = \frac{1}{2\gamma^2}\sqrt{\frac{2}{\pi\kappa}} \tag{E9}$$

$$\Omega_2(W) = \bar{R}_l + \frac{W^2}{2\gamma^2} \tag{E10}$$

$$\Lambda_2(W) = \frac{\kappa W^3}{\gamma^2} - \frac{\kappa^2 W}{4\gamma^2} - \left(\frac{1}{2} + \bar{R}_l\right)\kappa W. \tag{E11}$$

APPENDIX F:

MODES WITH U-VALUES

Mode	U	Mode	U	Mode	U	Mode	U	Mode	U
LP01	2.406	LP16	19.566	LP49	33.440	LP712	47.246	LP219	61.815
LP11	3.89	LP64	20.272	LP210	33.617	LP513	47.501	LP019	61.835
LP21	5.179	LP45	20.779	LP010	33.654	LP314	47.668	LP717	63.027
LP31	6.405	LP26	21.067	LP78	34.535	LP812	48.672	LP518	63.217
LP12	7.035	LP06	21.127	LP59	34.886	LP613	48.962	LP319	63.343
LP41	7.600	LP74	21.587	LP310	35.115	LP414	49.166	LP817	64.485
LP22	8.434	LP55	22.163	LP111	35.223	LP215	49.286	LP618	64.702
LP02	8.588	LP36	22.528	LP88	35.918	LP015	49.311	LP419	64.856
LP51	8.773	LP17	22.698	LP69	36.313	LP713	50.409	LP718	66.176
LP32	9.766	LP84	22.885	LP410	36.590	LP514	50.647	LP519	66.357
LP61	9.929	LP65	23.525	LP211	36.752	LP315	50.804	LP818	67.639
LP13	10.170	LP46	23.958	LP011	36.786	LP813	51.843	LP619	67.846
LP42	11.060	LP27	24.207	LP79	37.725	LP614	52.114	LP719	69.323
LP71	11.072	LP07	24.259	LP510	38.045	LP415	52.306	LP819	70.790
LP23	11.616	LP75	24.868	LP311	38.255	LP216	52.418		
LP03	11.727	LP56	25.363	LP112	38.354	LP016	52.442		
LP81	12.204	LP37	25.681	LP89	39.121	LP714	53.568		
LP52	12.325	LP18	25.829	LP610	39.483	LP515	53.792		
LP33	13.003	LP85	26.194	LP411	39.737	LP316	53.939		
LP14	13.302	LP66	26.747	LP212	39.866	LP814	55.009		
LP62	13.568	LP47	27.126	LP012	39.917	LP615	55.264		
LP43	14.352	LP28	27.345	LP710	40.905	LP416	55.444		
LP24	14.775	LP08	27.391	LP511	41.200	LP217	55.551		
LP72	14.793	LP76	28.112	LP312	41.394	LP017	55.573		
LP04	14.861	LP57	28.547	LP113	41.485	LP715	56.723		
LP53	15.672	LP38	28.829	LP810	42.313	LP516	56.935		
LP82	16.003	LP19	28.96	LP611	42.647	LP317	57.074		
LP34	16.196	LP86	29.461	LP412	42.882	LP815	58.171		
LP15	16.434	LP67	29.949	LP213	43.020	LP616	58.412		
LP63	16.969	LP48	30.286	LP013	43.049	LP417	58.582		
LP44	17.581	LP29	30.482	LP711	44.078	LP218	58.683		
LP25	17.924	LP09	30.523	LP512	44.352	LP018	58.704		
LP05	17.995	LP77	31.332	LP313	44.531	LP716	59.876		
LP73	18.246	LP58	31.721	LP811	45.496	LP517	60.077		
LP54	18.938	LP39	31.973	LP612	45.806	LP318	60.209		
LP35	19.368	LP110	32.092	LP413	46.024	LP816	61.329		
LP83	19.507	LP87	32.699	LP214	46.153	LP617	61.558		
		LP68	33.136	LP014	46.180	LP418	61.72		

REFERENCES

1. D. Gloge, "Weakly-guiding Fibers," *Applied Optics*, 10, 1971, 2252–2258.

2. A. Ghatak, and K. Thyagarajan, *Introduction to Fiber Optic: First South Asia Edition*, (Foundation Books, New Delhi for Cambridge University Press, Cambridge, UK, 1999), Ch. 8.

3. A.W. Snyder and J.D. Love, *Optical Waveguide Theory*, Kluwer Academic, Boston, 1983, Ch. 13.

4. A.W. Snyder and J.D. Love, *Optical Waveguide Theory*, Kluwer Academic, Boston, 1983, Sec. 20-3.

5. B. Saleh and M.C. Teich, *Fundamentals of Photonics*, John Wiley & Sons, Inc. New York, 1991, Ch.8.

6. A.Yariv, *Optical electronics in modern communications*, Oxford University Press, Oxford, England, 1997.

7. C. Hentschel, *Fiber Optics Handbook: An Introduction and Reference Guide to Fiber Optic Technology and Measurement Techniques, 3rd Edition*, Hewlett-Packard, Germany, 1989.

8. http://ceramoptec.com/industrial3.htm, Optran® PUV, Optran® PWF PCS-Fiber Specifications, April 13, 2004.

9. J.T. Foley, *Intermediate Optics Class Notes*, 2004.

10. K.L.Sreenivasan, *Fiber Optic Moisture Sensor Detection System*, Diagnostic Instrumentation and Analysis Library Masters Thesis Collection, 2003.

11. A.W. Snyder, C.Pask and, D.J. Mitchell "Light Acceptance Property of an Optical Fiber," *J. Opt. Soc. Am.*, Vol. 63, 1973, 59-63.

12. A.W. Snyder, "Asymptotic expressions for eigenfunctions and the eigenvalues of a dielectric or optical waveguide," *I.E.E.E. Trans. Microwave Theory Tech*, Vol 17**, (**1969)**,** 1130-8.

13. A.W. Snyder, "Excitation and Scattering of Modes on a Dielectric or Optical Fiber," *I.E.E.E. Trans. Microwave Theory Tech*, Vol 17**, (**1969), 1138-44.

14. J.R. Stern, M. Peace and R.B. Dyott, “Launching into Optical-Fibre Waveguide” *Electronics Letters*, Vol 6, No. 6, (1970), 160-2.

15. D. Marcuse “Excitation of the Dominant Mode of a Round Fiber by a Gaussian Beam,” *Bell System Tech. J.*, Vol 49, (1970), 1695-1703.